Paper I

Hydrocarbon sources of cold seeps off the Vesterålen coast, northern Norway

Sauer, S., Knies, J., Lepland, A., Chand, S., Eichinger, F., Schubert, C.J., 2015. Chemical Geology, 417: 371-382.

Hydrocarbon sources of cold seeps off the Vesterålen coast, northern Norway

Simone Sauer[a,b,*], *Jochen Knies*[a,b], *Aivo Lepland*[a,b], *Shyam Chand*[a,b], *Florian Eichinger*[c], *Carsten J. Schubert*[d]

Published in Chemical Geology

[a] Geological Survey of Norway, Trondheim, Norway

[b] CAGE - Centre for Arctic Gas Hydrate, Environment and Climate, The Arctic University of Norway, Tromsø, Norway

[c] Hydroisotop GmbH, Schweitenkirchen, Germany

[d] Eawag, Swiss Federal Institute of Aquatic Science and Technology, Kastanienbaum, Switzerland

* Corresponding author. Tel.: +47 73904169; *Email address*: simone.sauer@ngu.no

Abstract

We investigated active methane seeps in a water depth of 200 m in the Hola area off the coast of Vesterålen, northern Norway, to assess (1) hydrocarbon sources, (2) migration pathways and (3) the influence of hydrocarbon seepage on sediment pore water and water column chemistry. The seepage area is characterised by the presence of gas flares in the water column as revealed by hydro acoustic surveys and elevated methane concentrations of up to 42 nM ca. 5 m above the seafloor. Pore water analyses of three gravity cores from the seepage area show varying depths of the sulphate-methane-transition zone (SMTZ) between 80 cm and >250 cm indicating spatially heterogeneous methane ascent. The isotopic composition of methane ($\delta^{13}C$ from -40‰ to -63‰ and $\delta^{2}H$ from -191‰ to -225‰) and $\delta^{13}C$ depth profiles of methane and dissolved inorganic carbon show that the hydrocarbons are predominantly of thermogenic origin, consistent with $\delta^{13}C$ values of C_2 to C_4 hydrocarbons. Isotope data also indicate considerable biodegradation of propane. Seismic profiles from the study area reveal major faults and steeply dipping unconformities between the basement and overlying Mesozoic sedimentary rocks. We propose that these act as migration pathways for the hydrocarbons from late Jurassic to early Cretaceous source rocks.

1 Introduction

The release of methane at cold seeps has been the subject of recent investigations, because of its role in the marine carbon cycle and as a potential contributor to global warming (McGinnis et al., 2006; Skarke et al., 2014). Massive release of methane from the ocean may have played an important role in past climate change (Katz et al., 1999; Hesselbo et al., 2000), so it is important to understand the role of oceanic methane in the light of future climate change. Moreover, methane release has an effect on ocean acidification and de-oxygenation (Archer et al., 2009; Biastoch et al., 2011) and its seepage is a possible indicator of sub-seafloor hydrocarbon and gas hydrate reservoirs (Bünz et al., 2012).

Cold seeps generally form due to focused upward migration of both dissolved and/or gaseous hydrocarbons (Fischer et al., 2012) and they are common along passive and active continental margins worldwide (Mazurenko and Soloviev, 2003). Due to the amplification of climate warming in polar regions (Bekryaev et al., 2010), special interest has been paid to cold seeps in the Arctic in recent years. Water column gas flares of several hundred meters height occur, for example, off the coast of NW Spitsbergen where the gas hydrates in the sedimentary column are at the limit of stability (Hustoft et al., 2009; Westbrook et al., 2009; Sahling et al., 2014). It is hypothesized that increasing bottom water temperatures have reduced the extent of the gas hydrate stability zone (GHSZ) resulting in enhanced release of methane into the water column (Westbrook et al., 2009). Also on the Kara Sea shelf and the East Siberian Arctic shelf, gradually degrading offshore permafrost might cause methane emission to the atmosphere due to very shallow seeps (≤20 m water depth) (Shakhova et al., 2010; Portnov et al., 2013). On the Norwegian continental shelf and in the Barents Sea several gas seeps have been discovered (Solheim and Larsson, 1987; Hovland and Judd, 1988; Chand et al., 2012) which are interpreted to be related to deep-seated fault systems. Glacial unloading and erosion resulting in the re-activation of pre-

existing faults might have enabled fluid migration and escape of methane to the water column (Chand et al., 2012).

Our study area, the shelf offshore Vesterålen, is a barely investigated area compared to the main petroleum provinces in the Norwegian and Barents Sea where studies elucidating sources and fate of methane have been carried out already (Lammers et al., 1995; Chen et al., 2010). In the Hola area, on the Vesterålen shelf, only Chand et al. (2008) mentioned gas flares and the occurrence of bacterial mats, carbonate crusts and cold water coral reefs close to a seep site. However, the origin of the seep fluids and related geochemical and geological processes in this area have not been studied yet. In this study we investigated the cold seeps in the Hola area located offshore Vesterålen on the northern Norwegian shelf to assess (1) the potential hydrocarbon sources, (2) migration pathways and the(3) influence of fluids on sediment pore water and water column chemistry. For this purpose we mapped gas flare locations and seafloor structures related to the gas seepage. We further evaluated hydrocarbon sources by isotopic measurements of methane and higher molecular weight hydrocarbons in the sediment and studied the sediment pore water chemistry at the seep site.

2 Physiogeographic setting and geology

The shelf offshore Vesterålen, northern Norway, is relatively narrow and characterized by alternating shallow banks and deeper troughs which were formed during the last glaciation (Bøe et al., 2009) (Fig. 1B). The study area lies within the Hola trough, which is confined by the banks Vesterålsgrunnen to the NE and Eggagrunnen to the SW (Fig. 1B). The water depth in the Hola area varies between 75 m and 270 m below sea level (mbsl) (Fig. 1C) and the Norwegian Coastal Current (NCC) and the Norwegian Atlantic Current (NWAC) are the dominant water masses. The NCC flows along the coast coming from the southwest, whereas the NWAC follows the continental slope, coming from the southwest and

splitting into one branch towards Spitsbergen and one branch going eastward into the Barents Sea. In the Hola trough bidirectional tidal currents also strongly affect the bottom currents (Bøe et al., 2009).

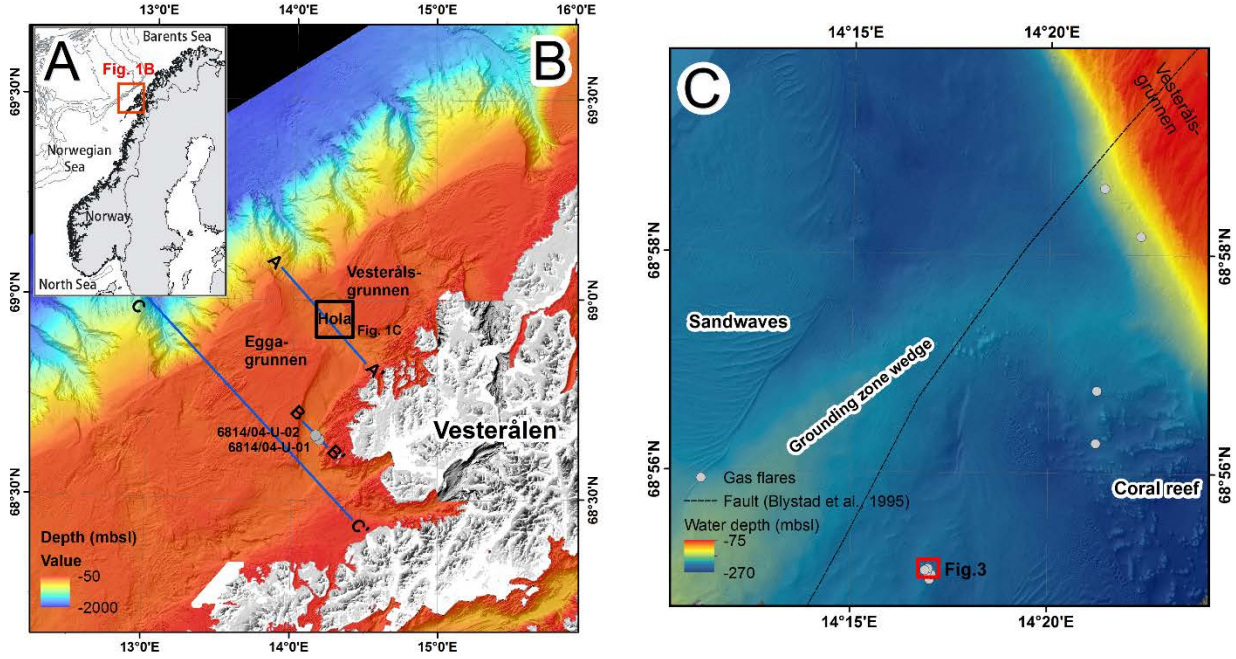

Figure 1: A) Map of Scandinavia and the Norwegian shelf, B) Depth-coloured shaded-relief bathymetry of the shelf offshore of Vesterålen (modified after Bøe et al. (2009)) with the Hola area indicated by the black box. The three blue lines mark seismic profiles and 2 grey dots show the location of two shallow wells (6814/04-U-01 and -02) (Smelror et al., 2001).C) Shaded-relief multibeam bathymetry of the Hola area with the red box indicating the area of highest gas flare activity (Fig. 3). The locations of gas flares detected during the HU Sverdrup II cruise in 2012 are indicated by grey dots and a regional fault (Blystad et al., 1995) is shown as dotted black line.

Basement ridges and large Cretaceous basins that run in an overall NE-SW direction, and are bounded by a complex extensional fault system, characterize the Lofoten-Vesterålen margin (Blystad et al., 1995; Loeseth and Tveten, 1996; Bergh et al., 2007; Færseth, 2012) (Fig. 2). The shelf in the study area comprises the sedimentary Ribban Basin which is located between the coast and the Utrøst Ridge (Blystad et al., 1995) (Fig. 2). The boundary between basement and sedimentary rocks in this part of the Norwegian shelf coincides with an angular unconformity and has been correlated to regional uplift in

Early to Early-Middle Jurassic times (Løseth, 1999). The succession offshore Vesterålen comprises Precambrian crystalline basement, Lower to Middle Jurassic sandstones with coal-rich layers, Upper Jurassic, sandy calcareous mudstones and Lower to Upper Cretaceous clay-, silt- and sandstones with organic rich intervals (Henningsen and Tveten, 1998).

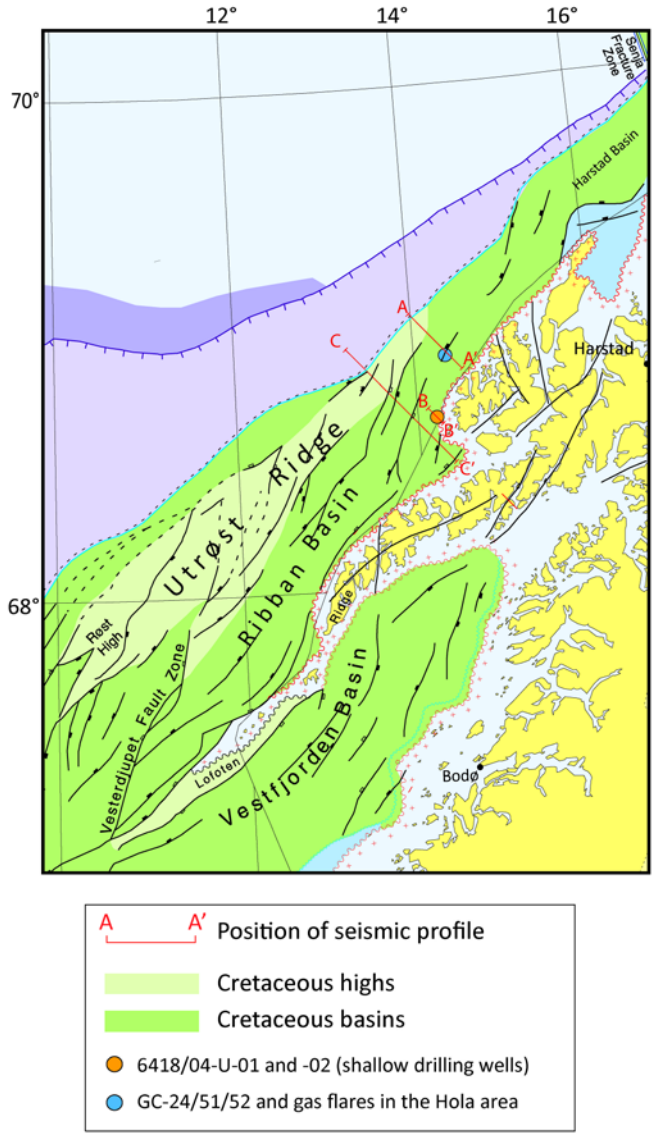

Figure 2: Geological structures on the Lofoten-Vesterålen margin (modified after Blystad et al. (1995)). The blue dot shows the location of gas flares in the Hola area and the orange dot shows shallow wells 6814/04-U-01 and -02 (Smelror et al., 2001). Red lines indicate seismic profiles A, B and C which are shown in Fig. 9.

The Quaternary sediment cover was formed during several glacial cycles (Ottesen et al., 2002; Ottesen et al., 2005a) and on most parts of the shelf it is less than 25 m thick and comprised of till. Fine grained glaciomarine sediments and Holocene sands occur above the till in the troughs (Bøe et al., 2009) and the uppermost approximately 10 cm comprise a layer of gravel and cobbles representing a lag deposit in the Hola trough. During glacial periods the shelf was protected from the inland ice by the high mountain range of the Lofoten-Vesterålen Islands (Rise et al., 2012) thereby confining large ice streams to Andfjorden and Vestfjorden (Ottesen et al., 2005a; Ottesen et al., 2005b; Vorren et al., 2013). The latest compilation of deglaciation events on the Lofoten-Vesterålen shelf suggests that deglaciation in this area took place between ca. 24 cal ka BP (ice at shelf edge) and ca. 16 cal ka BP (ice at present coastline of Vesterålen) (Vorren et al., 2015). During deglaciation the ice came to a halt several times producing grounding zone wedges. Vorren et al. (2015) suggest that the grounding zone wedge crossing the Hola area (Fig. 1C) was formed at ca. 18-17.5 cal ka BP. Other characteristics of seabed morphology in the Hola area include the occurrence of large sandwaves and cold water coral reefs (Bøe et al., 2009) (Fig. 1C).

3 Methods and materials

3.1 Acoustic investigations and coring

Acoustic and geochemical data were collected during 3 research cruises in 2012 and 2013. Multibeam echosounder data were collected in 2012 by the Norwegian Defence Research Establishment (FFI) using a Kongsberg Maritime EM710 mounted on FFI's research vessel HU Sverdrup II. It is a 0.5x 1.0 degree system and has an operating frequency of 70 - 100 kHz. With water depths of approximately 350 m the spatial resolution is 3 to 4 m. The multibeam data were processed using Fledermaus FMGT and Fledermaus MidWater package. In April 2013, an Autonomous Underwater Vehicle (AUV) survey was

conducted during a HU Sverdrup II cruise. FFI's AUV (HUGIN) was equipped with the High resolution Interferometric Synthetic Aperture Sonar (HISAS 1030). The HUGIN was flown ~10 m above the seafloor. The HISAS system is capable of providing very high resolution images and detailed bathymetry of the seabed. The system has a range-independent resolution of approximately 3x3 cm out to a distance of 200 m from both sides of the AUV at a speed of 2 m/s. The R/V Helmer Hansen cruise in April 2013 provided single beam echosounder data from a Simrad ER-60 at frequencies of 18 kHz, 38 kHz and 120 kHz. Furthermore, 3 gravity cores were collected and water samples were taken during a CTD cast (Table 1) which also logged temperature, salinity and O_2 content. 2D industry airgun seismic data lines were available from the study area through RWE Dea Norge. The 2D seismic data are of low resolution (50-60 Hz) with large spacing between individual lines and collected in different acquisition campaigns.

Table 1: Gravity core and CTD locations.

Station name	Latitude (N)	Longitude (E)	Water depth (m)	Device	Recovery (cm)
HH13-GC 24	68.9174	14.2851	220	gravity corer	235
HH13-GC 51	68.9179	14.2858	222	gravity corer	312
HH13-GC 52	68.9178	14.2860	223	gravity corer	260
HH13-CTD 209	68.9178	14.2839	220	CTD	

3.2 CTD and water samples

Water column salinity, temperature and oxygen data were recorded with a Seabird SBE 911 + CTD equipped with an SBE 43 (Seabird Electronics) oxygen sensor. Water samples from different depths were collected during the upcast of the CTD station with 10 l Niskin bottles mounted on a rosette sampler. The seawater was transferred into 500 ml serum bottles from the Niskin bottles via a rubber tube. The tube was placed at the bottom of the bottle to prevent the formation of bubbles. The bottles were filled until overflow, sodium hydroxide pellets were added, and the bottles sealed with a rubber stopper and an aluminium crimp seal and stored at 4°C until further onshore analyses.

3.3 Sediment pore water sampling

The gravity cores were sampled for sediment pore water on deck at ca. 5°C air temperature using the rhizon technique (Rhizon micro suction samplers: 10 cm, 0.15 µm porous polymer, Rhizosphere Research) (Schulz, 2006). 3.8 mm holes were drilled into the plastic liner with an electric drill at intervals of 20 cm, the rhizons were inserted with attached three way luer lock stopcocks and 10 ml syringes. To create a vacuum inside the syringes they were kept open with a spacer. After 30 min to 8h the syringes had filled with 10 ml pore water.

For methane (CH_4) sampling, holes with a diameter of 1.5 cm were drilled into the plastic liner at intervals of 20 cm in between the rhizon holes. 3 ml of sediment were taken using a 5 ml syringe with the luer tip removed. The sample was transferred to a 20 ml serum vial containing 2 glass beads and 6 ml NaOH (2.5%) to prevent microbial activity. The vial was immediately closed with a septum and an aluminium crimp seal and stored at 4°C until further analyses. For instant analysis of dissolved iron (Fe^{2+}), 1 ml of pore water was extracted with a 1 ml disposable syringe through the 3-way stopcock after the syringes had filled with a few millilitres of pore water. The remaining pore water was used for onboard analysis of phosphate (PO_4^{3-}) and onshore analysis of major anions (Cl^-, SO_4^{2-}) and calcium (Ca^{2+}), ammonium (NH_4^+), sulphide (HS^-) and $\delta^{13}C$ of dissolved inorganic carbon (DIC). For onshore analyses dilutions were prepared from the pore water samples. 40 µl of plain pore water were diluted with 3960 µl of deionized water (1:100) for anion determination by ion chromatography (IC) and placed into 4 ml glass vials with cap and gas-tight septum. For major element determination by inductively coupled plasma – atomic emission spectrometry (ICP-AES) 1 ml of pore water was added to 9 ml of 1 vol% HNO_3 (1:10) to prevent precipitation of minerals and adsorption onto the walls of the sample vial. For $\delta^{13}C_{DIC}$ determination a 1.5 ml glass vial was filled without headspace. 1 ml of pore water was pipetted into a 2 ml Eppendorf vial containing 100 µl of 5% $ZnCl_2$ solution for photometric HS^-

determination. 2 ml of pore water were filled into cryovials and frozen for determination of NH_4^+. All samples (except for NH_4^+) were kept refrigerated at 4°C until further onshore analyses.

3.4 Analyses

3.4.1 On-board analyses

Fe^{2+} was determined photometrically using a Shimadzu UVmini-1240 UV-Vis Spectrophotometer at 560 nm after forming a violet colour complex with a commercial ferrospectral solution (Collins et al., 1959). For photometric PO_4^{3-} analysis after Murphy and Riley (1962) 10 µL of conc. HCl was added to 1 mL of plain sample and left overnight to remove all H_2S which would disturb the reaction forming the colour complex. Ammonium molybdate solution and ascorbic acid solution were added to 1 ml of plain sample. Orthophosphate ions form a complex in acid solution and in the presence of molybdate ions. Ascorbic acid then reduces the complex to form phosphomolybdenum blue, which is subsequently detected photometrically at 880 nm with a Shimadzu UVmini-1240 UV-Vis Spectrophotometer.

3.4.2 Onshore analyses

Dissolved sulphide ($\Sigma H_2S = H_2S + HS^- + S^{2-}$) was measured on the $ZnCl_2$ preserved pore water samples by the photometric methylene blue method (Cline, 1969) on a DR5000 UV-VIS Spectrophotometer at University of Bremen, Germany. Ammonium was detected with a flow injection teflon tape gas separator technique after Hall and Aller (1992) at the University of Bremen, Germany. The anions chloride (Cl^-) and sulphate (SO_4^2) were determined using a Dionex ICS - 1100 Ion Chromatograph with a Dionex AS-DV autosampler and a Dionex IonPac AS23 column at the Geological Survey of Norway (relative standard deviation: ± 0.7%, 1 σ, n =10). Cations (e.g. Ca^{2+}) were measured on an ICP-AES PerkinElmer 4300 Dual View with a Cross flow GemTip nebulizer at the Geological Survey of Norway (relative standard deviation ± 5% , 1σ). Methane concentration in the sediment/pore water samples was measured on the headspace of the 20 ml serum vials using Gas Chromatography (GC). The

measurements were performed at the Swiss Federal Institute of Aquatic Science and Technology using an Agilent Gas Chromatograph G1530N with a flame ionization detector. The relative standard deviation of the CH_4 measurements based on repeated measurements of a calibration standard is $\pm$ 2.9% (1σ). For the measurement of water column CH_4 concentrations a 100 ml headspace of pure N_2 was introduced into the 500 ml serum bottles. Equilibration was achieved by shaking the bottle, placing it in an ultrasonic bath for 15 min, and waiting over night before analysing the CH_4 headspace concentration using an Agilent Gas Chromatograph G1530N with a flame ionization detector at the Swiss Federal Institute of Aquatic Science and Technology. The CH_4 concentration for both water column and sediment pore water was calculated by adding the headspace CH_4 concentration (which was measured on the gas chromatograph) to the CH_4 concentration in the fluid/sediment which was calculated using the Bunsen coefficient from Yamamoto et al. (1976) taking into account temperature and salinity. For CH_4 concentration in the pore water the calculated CH_4 concentration per sediment volume was corrected with an assumed constant sediment porosity of 0.8 (Haeckel et al., 2001).

The stable carbon isotopes of methane (C_1), ethane (C_2), propane (C_3), *i*-butane (i-C_4) and *n*-butane (n-C_4) and hydrogen isotopes of methane were analysed at Hydroisotop GmbH, Germany. For the analyses an aliquot of the headspace gas was taken with a 10 ml gastight syringe and injected into 20 ml headspace vial filled with helium , which is suitable for the purge&trap autosampler. In the purge&trap autosampler (MessTechnik GmbH) the content of the bottle is flushed with He and trapped 20 minutes on the absorption material at -120°C. After fast heating up to 200°C the gas mixture is transfered to the GC-MS-IRMS system (Thermo Fischer Scientific GmbH). The GC (Trace Ultra) separates C_1-C_4 gases from each other which are then transferred to the combustion/pyrolyses interface for conversion of hydrocarbons to CO_2 or H_2 for carbon and hydrogen stable isotope measurements using an isotope ratio mass-spectrometer (IRMS, DeltaV Advantage) equipped with a highly evacuated electron impact ion source analyser system. The isotopic composition ($\delta^{13}C$ and $\delta^{2}H$) is reported in ‰ (δ-values) against the

international standards Vienna Pee Dee Belemnite (VPDB) for carbon and Vienna Standard Mean Ocean Water (VSMOW) for hydrogen, according to equations:

$$\delta^{13}C_{VPDB} = \frac{(^{13}C/^{12}C)_{sample} - (^{13}C/^{12}C)_{VPDB}}{(^{13}C/^{12}C)_{VPDB}} \text{x1000 (‰) and}$$

$$\delta^{2}H_{VSMOW} = \frac{(^{2}H/^{1}H)_{sample} - (^{2}H/^{1}H)_{VSMOW}}{(^{2}H/^{1}H)_{VSMOW}} \text{x1000 (‰).}$$

The analytical precision of $\delta^{13}C$ and $\delta^{2}H$ was $\pm$ 1.5‰ (1σ) and 10‰ (1σ), respectively. Methane carbon isotopic composition ($\delta^{13}C$-CH_4) was also determined with a trace gas analyser connected to a mass spectrometer (GV Instruments) at the Swiss Federal Institute of Aquatic Science and Technology.

The stable carbon isotopes of dissolved inorganic carbon ($\delta^{13}C$-DIC) in the pore water samples were determined on the CO_2 liberated from the water after acidification with phosphoric acid. Measurements were done with a gas bench coupled to a Delta V Plus mass spectrometer (Thermo, Switzerland) at ETH Zürich and at EAWAG using a multiflow connected to an Isoprime mass spectrometer (GV Instruments, UK). The standard deviation of the $\delta^{13}C$-DIC measurements was $\pm$ 2.5‰ (1σ).

4 Results

4.1 Gas flare mapping

The locations of gas flares in the Hola area were identified using multi-beam and single-beam water column echosounder data collected during 2 cruises (HU Sverdrup II cruise in 2012, R/V Helmer Hansen cruise in spring 2013) (Fig. 3). The gas flares concentrated in an area close to two seafloor highs, assumed to be coral mounds (Chand et al., 2008), and an area of carbonate crusts which covers ca. 2000 m^2 of the seafloor (Fig. 3). Some weaker flares were also observed further to the northeast of this area in the coral reef field and close to the edge of the Hola trough (Fig. 1C) during the HU Sverdrup II

cruise in 2012. These flares were, however, not found active during the R/V Helmer Hansen cruise in spring 2013.

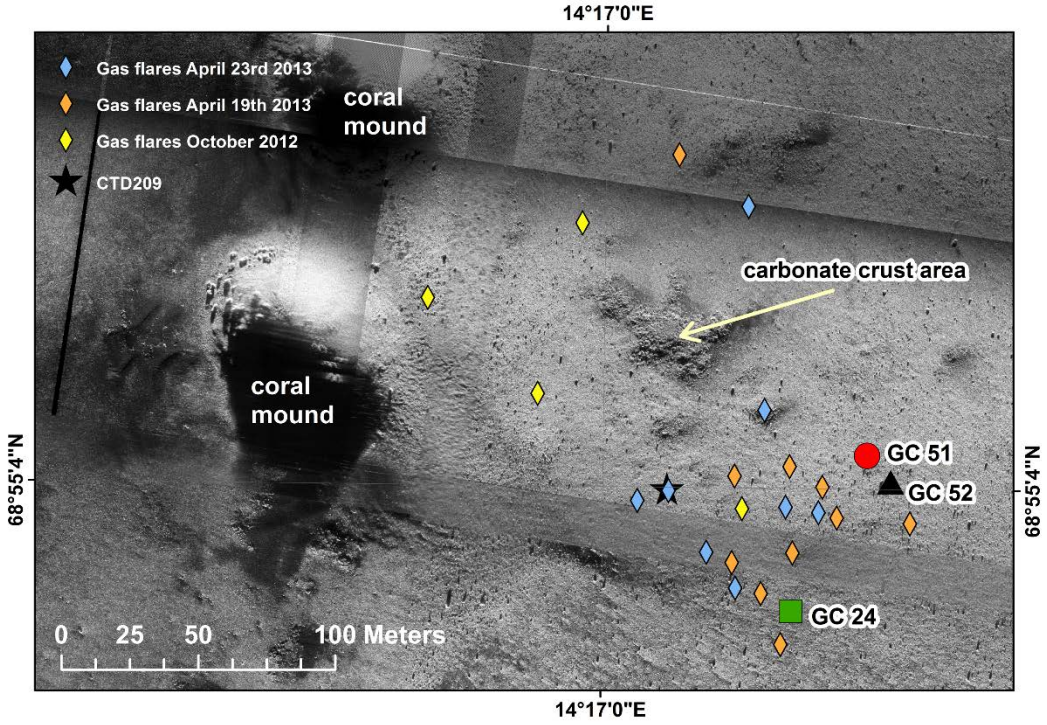

Figure 3: High resolution synthetic aperture sonar (HiSAS) image of the seafloor acquired by AUV Hugin. The two round features on the left are coral mounds and the darker area on the right is a carbonate crust area of ca. 2000 m^2. Gas flare locations have been identified using multibeam (yellow diamonds) and single beam (orange and blue diamonds) echosounder water column data. The star represents the CTD location and the square, dot and triangle are gravity core (GC) positions.

4.2 Methane concentration in the water column

Data from a CTD cast (CTD 209) showed a sea surface temperature of ca. 6 °C and salinity of 34.7‰ (Fig. 4A) in the Hola area. With increasing water depth the temperature and salinity increased by 0.7°C and 0.3‰, respectively. Oxygen concentrations decreased from 5.8 ml/l at the sea surface to 5.4 ml/l above the seafloor (Fig. 4A). At this site (CTD 209, Fig.3) methane was released to the water column from the sediment as gas bubbles which produced a signal in the water column echosounder data (Fig. 4C, 18 kHz). As there were no bubbles detected shallower than ca. 125 m (Fig. 4C, 18 kHz) it is assumed

they dissolved and did not reach the sea surface. Dissolved methane concentration was 20 nM in 50 m water depth and increased to 42 nM just above the seafloor (Fig. 4B). During CTD cast 209 the lowermost two water samples were taken from within a gas flare (Fig. 4C).

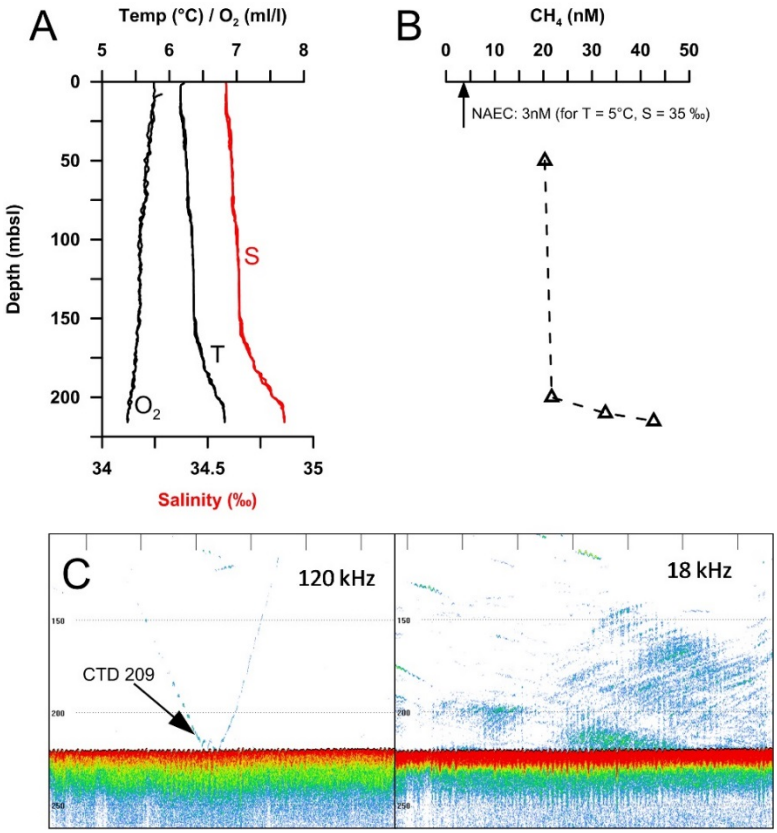

Figure 4: A) Temperature (T), salinity (S) and oxygen (O_2) profiles of CTD 209 (location is indicated in Fig. 3); B) Dissolved methane concentration in the water column measured on 4 discrete water samples taken during CTD cast 209. The arrow indicates the normal atmospheric equilibrium concentration (NAEC) for methane (Libes, 2009) for T = 5°C and S = 35‰, C) CTD location observed on 120 kHz echosounder data (left) coincides with bubble plumes observed on 18 kHz echosounder data (right).

4.3 Sediment pore water geochemistry

We analysed the concentration of anions and cations in 40 pore water samples from three gravity cores HH13-GC 24, HH13-GC 51 and HH13-GC 52 (hereafter referred to as GC 24, GC 51 and GC 52) (locations marked in Fig. 3) and the results are presented in Fig. 5 .

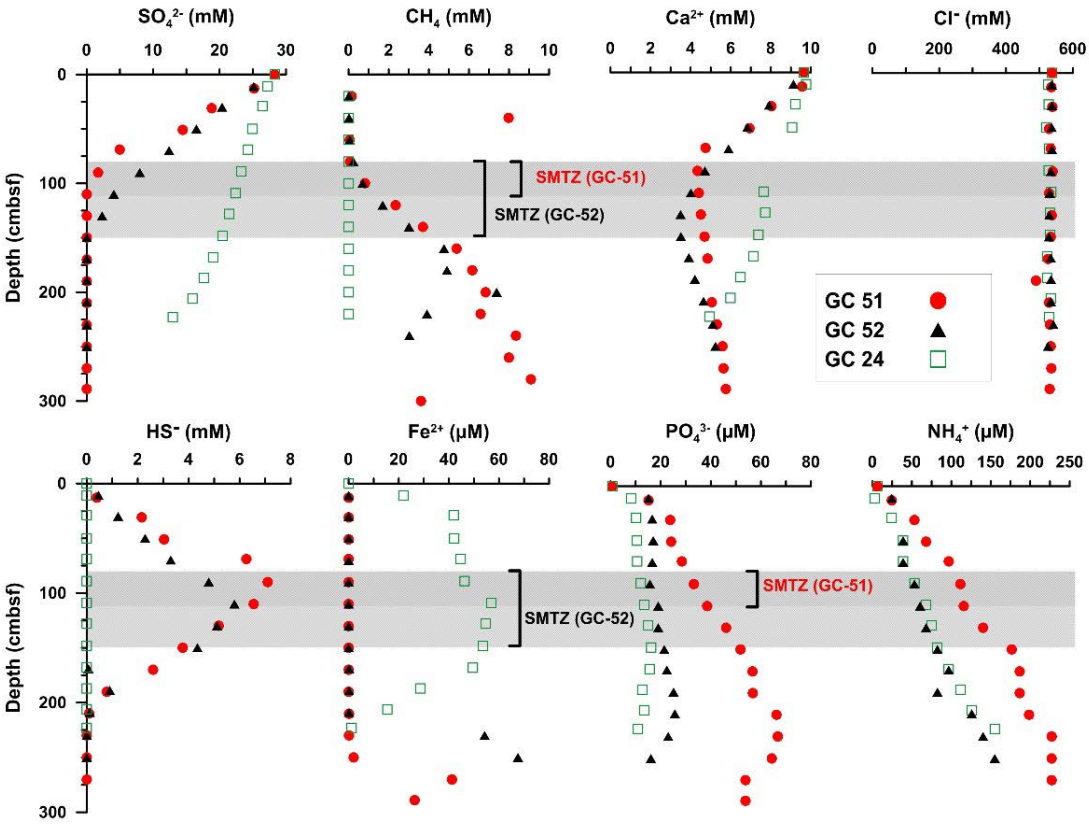

Figure 5: Pore water profiles of the three gravity cores GC 24 (green open squares), GC 51 (red filled circles) and GC 52 (black filled triangles). The grey bands indicate the depth and thickness of the sulphate-methane-transition-zone (SMTZ) in core GC 51 and GC 52. The upper boundary of the SMTZ is constrained by the increase in CH_4 and the lower boundary by the depletion of SO_4^{2-}.

Sulphate concentrations decreased from 28 mM (seawater concentration, (Claypool and Kaplan, 1974)) at the top of the core to below detection limit at 110 cm sediment depth in GC 51 and at 150 cm in GC 52. In GC 24 SO_4^{2-} decreased from 28 mM to 13 mM at the bottom of the core (core length 235 cm). This concentration gradient suggests a complete depletion of SO_4^{2-} in the depth range between 250 cm and 400 cm in GC 24 (Fig. 5). Dissolved CH_4 concentrations started to increase at 80 cm in both GC 51 and GC 52 reaching maximum values of 9 mM and 7.4 mM, respectively.

The sulphate-methane-transition-zone (SMTZ) (e.g. Iversen and Jørgensen, 1985), i.e. the depth between CH_4 increase and SO_4^{2-} depletion, spanned a zone between 80 cm and 110 cm sediment depth

in GC 51 and 80 cm to 150 cm sediment depth in GC 52 (Fig. 5). However, one sample of GC 51 with 8 mM CH_4 at 50 cm depth (<0.15 mM in the sample above and below) did not fit into the observed pattern (Fig 5). This could be an analytical error or newly introduced CH_4 gas in this depth, for example by horizontal CH_4 migration. In sediment core GC 24 maximum dissolved CH_4 concentrations reached 12 µM . HS^- concentrations were at a maximum at the SMTZ with 7 mM in GC 51 and 6 mM in GC 52 and decreased upward and downward (Fig. 5). In core GC 24 HS^- was below the detection limit. Fe^{2+} was present throughout the whole core of GC 24 with values up to 57 µM. Fe^{2+} concentrations in core GC 51 and GC 52 started to increase below the depth where HS^- was depleted (230 cm in GC 51 and 209 cm in GC 52) (Fig. 5). In core GC 51 and GC 52 Ca^{2+} concentrations followed the SO_4^{2-} concentration pattern and showed a minimum of 4.3 mM and 3.5 mM, respectively, at the depth of the SMTZ. This is a 56% and64 % depletion compared to bottom water concentrations. Below the SMTZ, Ca^{2+} concentrations rose again (Fig. 5). In core GC 24 there was just a gradual decrease of Ca^{2+} with depth which followed the SO_4^{2-} concentration (Fig. 5). Phosphate and ammonium concentrations gradually increased with depth in all cores. GC 24 and GC 52 showed similar profiles of PO_4^{3-} concentration with a maximum of 16 µM and 26 µM and NH_4^+ concentrations with a maximum of 155 µM (Fig. 5). The concentrations in GC 51 were slightly higher with up to 65 µM (PO_4^{3-}) and 230 µM (NH_4^+). Chloride (Cl^-) concentrations were constant with depth with average concentrations between 529 mM (GC 24) and 535 mM (GC 52).

4.4 Stable isotopes of hydrocarbon gases and dissolved inorganic carbon

We analysed 23 gas samples from two gravity cores (GC 51 and GC 52) for their stable carbon isotope composition of methane ($\delta^{13}C$-CH_4) (Fig. 6). $\delta^{13}C$-CH_4 values ranged between -53‰ and -63‰ in core GC 51 and between -40‰ and -54‰ in core GC 52. In both cores the lowest $\delta^{13}C$-CH_4 values were found at the bottom of the SMTZ (Fig. 6). Below the SMTZ $\delta^{13}C$-CH_4 values increased gradually from -63‰ to -53‰ in GC 51 and much less in GC 52 (from -54‰ to -52‰). In GC 52 there was a strong shift in $\delta^{13}C$-CH_4 from -54‰ at 120 cm to -40‰ at 50 cm. This shift was only minor (from -63‰ to - 60‰) in GC 51.

The stable carbon isotopic composition of dissolved inorganic carbon (δ^{13}C-DIC) was analysed on all 40 pore water samples. The lowest values were -12‰ in core GC 51 and -19‰ in GC 52 at a depth of around 90 cm. Further downcore, δ^{13}C-DIC gradually increased up to 18‰ in GC 51 and 19‰ in GC 52. In contrast, in GC 24 δ^{13}C-DIC decreased from -2‰ to -20‰ towards the bottom of the core (Fig. 6). The δ^{13}C of the higher molecular weight hydrocarbons (ethane, propane, *i*- butane, *n*-butane) and the δ^{2}H of methane were measured on 3 samples from core GC 51 and 3 samples from GC 52 (Table 2). The δ^{13}C increased with increasing number of carbon atoms (except for butane): δ^{13}C-CH_4 varied between -60‰ and -52‰, δ^{13}C-C_2H_6 between -37‰ and -33‰ and δ^{13}C-C_3H_8 -16‰ and -7‰. However, the values of δ^{13}C-i-C_4H_{10} (-30 to -26‰) and δ^{13}C-n-C_4H_{10} (-29 to -22‰) were lower again. The values for δ^{2}H-CH_4 varied between -191‰ and -225‰ (Table 2).

Table 2: Results of the analyses of δ^{13}C of the C_1 to C_4 hydrocarbons and δ^{2}H of CH_4.

	δ^{2}H (‰ V-SMOW)	δ^{13}C (‰ V-PDB)				
Sample	CH_4	CH_4 (C_1)	C_2H_6 (C_2)	C_3H_8 (C_3)	*i*-C_4H_{10} (*i*-C_4)	*n*-C_4H_{10} (*n*-C_4)
GC 51-140 cm	-218	-60.0	-34.4	-14.9	-29.4	-22.4
GC 51-220 cm	-225	-56.1	-36.5	-16	-28.8	-22.5
GC 51-300 cm	-223	-52.7	-34.4	-12.1	-29.4	-24.8
GC 52-140 cm	-191	-54.4	-33.7	-9.5	-29.7	-25.2
GC 52-180 cm	-212	-53.5	-34.6	-13.2	-26.0	-26.3
GC 52-240 cm	-222	-52.3	-34.0	-7.0	-27.0	-29.1

5 Discussion

Characterization of hydrocarbon seepage

5.1 Water column

In settings of vigorous seepage such as Hydrate Ridge and the Håkon Mosby Mud Volcano (HMMV) high dissolved CH_4 concentrations in the water column of up to 3 µM (Suess et al., 1999) and up to 10 µM (Sauter et al., 2006), respectively, have been reported. In other active seep sites the reported dissolved CH_4 concentrations typically range between 20-200 nM, e.g. on the SW-Spitsbergen shelf (Damm et al.,

2005), in the Eel River Basin (Valentine et al., 2001), in the Davis Strait (Punshon et al., 2014) or the South Kara Sea (Portnov et al., 2013). In the Hola area, the maximum measured dissolved CH_4 concentration in the water column is 42 nM (Fig. 4B), which lies at the lower end of reported values for cold seeps. Also the density of flares is low in the Hola area compared to sites such as the continental margin west of Spitsbergen with several hundred active flares (Westbrook et al., 2009; Sahling et al., 2014). The lack of gas flare reflections in water column echosounder data at the sea surface and decreasing CH_4 concentrations towards the sea surface suggest that the majority of CH_4 emitted from the sediment at our study site is probably dissolved and dispersed in the water column (McGinnis et al., 2006), which may be aided by relatively strong currents in the area.

5.2 Sediment pore water geochemistry

5.2.1 Variable depth of the SMTZ: Evidence for focused fluid flow

The upward migration of methane towards the sediment-water interface produces steep geochemical gradients in the sediment pore water (Fischer et al., 2012) which are spatially very heterogeneous across the Hola seep area. The transition between decreasing SO_4^{2-} and increasing methane, the SMTZ, is the region of anaerobic oxidation of methane (AOM), where a consortium of anaerobic methane oxidising archaea (ANME) and sulphate reducing bacteria mediate the overall reaction (Reeburgh, 1976; Hinrichs et al., 1999; Boetius et al., 2000; Orphan et al., 2001):

$$CH_4 + SO_4^{2-} \rightarrow HS^- + HCO_3^- + H_2O. \qquad \text{(reaction 1)}$$

Sulphate depletion and the depth of the SMTZ is usually controlled by the flux of organic matter to the sediment (e.g. Canfield, 1991). However, in the Hola area there is a large variation of the SO_4^{2-} gradients in the three closely-located gravity cores (maximum distance between cores: 60 m) and it is unlikely that the availability of degradable organic matter is so variable and can create these differences. It is more likely that variable upward flux of CH_4 determines the depth of the SMTZ and the gradient of SO_4^{2-}

depletion (Borowski et al., 1996; Hensen et al., 2003) in the sediment pore water of the Hola area. Thus, a SMTZ close to the sediment-water-interface means a higher CH_4 flux (as in GC 51) whereas a deeper SMTZ means lower CH_4 flux (as in GC 24). This difference in SMTZ depth of at least 1.5 m implies a strong spatial heterogeneity in CH_4 flux in the Hola area. Hence, we assume a localized nature of fluid flow in this region with fluid pathways probably along fractures or faults and with core GC 51 likely closest to a fluid conduit and GC 24 with a deeper SMTZ further away. At other cold seep sites such as the Eel River Basin and the Hydrate Ridge, the SMTZ depth is as shallow as 10 cmbsf (Gieskes et al., 2005) and even 5 cmbsf at the Makran Accretionary Prism (Fischer et al., 2012). This suggests that we sampled at greater distance to the active seep site in Hola. At the sites of bubble escape, the SMTZ should be at the seafloor, whereas at the sites of our gravity cores, the combined effect of lower methane flux and AOM in the sediment prevents any methane from reaching the seafloor and thus no gaseous methane escape is taking place.

The ascent of CH_4 and associated AOM can result in the precipitation of authigenic carbonate at the SMTZ due to the production of HCO_3^- (reaction 1) (Aloisi et al., 2002; Luff and Wallmann, 2003; Moore et al., 2004; Ussler III and Paull, 2008). The concentration minima of pore water Ca^{2+} in both cores GC 51 and GC 52 coincide with the depth of the SMTZ (Fig. 5) and suggest $CaCO_3$ precipitation at these depths. Furthermore, the coinciding depletion of HS^- (diffusing downward from the SMTZ) and Fe^{2+} (diffusing upward) at 230 cm in GC 51 and 210 cm in GC 52 (Fig. 5), indicates the precipitation of an iron sulphide phase below the SMTZ in these cores.

Altogether, our pore water profiles suggest different CH_4 fluxes from below in the three gravity cores illustrating the spatial variability of hydrocarbon seepage in the Hola area. Additionally, the precipitation of a calcium carbonate phase and an iron sulphide phase is suggested by the pore water profiles. The depth of these precipitation horizons is influenced by the flux of CH_4 at each site, which determines the depth of the SMTZ.

5.2.2 Decomposition of organic matter

In high productivity regions like the Bering Sea a SMTZ depth of 6 m has been reported by Wehrmann et al. (2011). In contrast, our study area in Hola is not a high productivity region, but still the SMTZ depths are significantly shallower. This supports the notion that in the Hola area SMTZ depth is mainly controlled by ascending methane from a deeper source instead of in-situ microbial methanogenesis fuelled by organic matter input. This is further supported by low concentrations of ammonium and phosphate in the pore water (Fig. 5). Ammonium and phosphate are released into the pore water during organic matter degradation (Froelich et al., 1979) and their concentration usually increases with depth. AOM does not generate any NH_4^+. We assume low rates of organic matter remineralisation in the Hola area since the NH_4^+ concentrations are more than a magnitude lower than compared to high-productivity regions like offshore Namibia or the Aru Sea (Indonesia) (Niewöhner et al., 1998; Alongi et al., 2012). Also PO_4^{3-} concentrations are up to 6 times lower than offshore Namibia (Niewöhner et al., 1998). Low rates of organic matter remineralisation supports our assumption that ascending methane exerts the strongest control on pore water geochemistry in the Hola area.

5.3 Source of hydrocarbon gases in Hola sediments

5.3.1 $\delta^{13}C$ of methane and dissolved inorganic carbon

In the marine environment the most common sources of methane are either the thermocatalytic breakdown of complex organic matter at temperatures above 150°C (e.g. Clayton 1991) producing thermogenic methane, or microbial (archaeal) methanogenesis (Judd, 2004) at temperatures below 80°C (Rice and Claypool, 1981) producing microbial methane. One of the pathways of microbial methanogenesis in marine sediments is by 'carbonate reduction' or hydrogenotrophic methanogenesis:

$HCO_3^- + 9H^+ + 8e^- \rightarrow CH_4 + 3H_2O$ (reaction 2, (e.g. Whiticar, 1999))

Another methanogenic pathway is the fermentation of methyl-type substrates (acetate). However, in the marine environment sulphate reducing bacteria can outcompete the methanogens for acetate as a substrate which may results in the dominance of carbonate reduction methanogenesis in some areas (Whiticar, 1999). The link between DIC and CH_4 as described in reaction 2 allows to deduce information about CH_4 source from the profiles of δ^{13}C-DIC and δ^{13}C-CH_4.

Generally, DIC in pore water can be derived from different sources which have distinctly different δ^{13}C values: buried seawater DIC has a δ^{13}C of around 0‰ (Walter et al., 2007), metabolic DIC is generated from mineralizing marine organic matter which has a δ^{13}C between −35‰ and −16‰ (Goericke and Fry, 1994) and AOM can produce even lower δ^{13}C-DIC values, e.g. -55‰ (Chen et al., 2010).

In sediment cores GC 51 and GC 52 δ^{13}C-DIC values reach a minimum value (-12‰ and -19‰) at and just above the SMTZ (Fig. 6). Thus, we interpret DIC here to be a mixture of buried seawater DIC and the product of either organic matter remineralisation or AOM. As low nutrient concentrations suggest low rates of organic matter remineralisation, probably AOM is the main contributor of isotopically light DIC. Downcore, below the SMTZ, δ^{13}C-DIC gradually increased up to around 18‰ in GC 51 and 19‰ in GC 52. Whiticar (1999) suggests that such an increase can be caused by microbial methanogenesis ('carbonate reduction') preferentially using the isotopically light DIC. δ^{13}C-DIC values above 0‰ should be an indication of removal of ^{13}C depleted DIC from the DIC pool because these values cannot be produced by the mixing of the proposed sources which have δ^{13}C-DIC values ≤ 0‰ (seawater δ^{13}C-DIC around 0‰ , metabolically produced DIC: δ^{13}C < 0‰). Hence, the gradual increase of δ^{13}C-DIC with depth probably reflects carbonate reduction methanogenesis which enriches the remaining DIC in ^{13}C over time. The presence of methanogenesis in shallow sediments at seep sites has also been proposed by other studies based on measurements of rates of methanogenesis (Orcutt et al., 2005) and biomarker analyses (Feng et al., 2014). However, we do not expect in-situ microbial methanogenesis to be a major contributor to

the overall methane budget in Hola sediments. Rather focussed flow from deeper sources, as inferred from the variable SO_4^{2-} gradients, dominates the methane budget. In this regard, the high values of δ^{13}C-DIC of up to +19‰ are unusual in such shallow sediment depth and where low rates of organic matter degradation and microbial methanogenesis are expected. Yet, a possible explanation may be low concentrations of DIC in the zone of methanogenesis, which could cause a strong enrichment of ^{13}C in the remaining DIC pool even with comparably low rates of methanogenesis.

If all the methane in the pore water was produced only by in situ microbial methanogenesis via carbonate reduction, the expected δ^{13}C-CH_4 profile would run parallel to the δ^{13}C-DIC profile, i.e. they would show the same gradients below the SMTZ due to a constant fractionation factor during methanogenesis (Whiticar, 1999). This has been observed for example in northern Cascadia Margin sediments (Heuer et al., 2009) where δ^{13}C-DIC and δ^{13}C- CH_4 run parallel below the SMTZ over an interval of more than 100 m. However, in the Hola area the gradients of δ^{13}C-DIC and δ^{13}C- CH_4 below the SMTZ are different (Fig. 6). In core GC 51 (GC 52) δ^{13}C-DIC increases by 20‰ (26‰) 1 m below the SMTZ whereas the increase in δ^{13}C- CH_4 in the same interval is only 5‰ (2‰) (Fig. 6). This suggests a considerable contribution of methane from deeper sources other than in-situ microbial methanogenesis. Especially in core GC 52 the δ^{13}C- CH_4 profile, which is almost constant below the SMTZ, points to a thermogenic methane source from below, because a uniform δ^{13}C- CH_4 signal is expected from ascending thermogenic methane which is only expected to change its isotopic composition when the methane is oxidised at the SMTZ. This is observed in core GC 52 by a 14‰ isotope shift in the depth between 130 cm and 50 cm.

In core GC 51, below the SMTZ, the gradient of δ^{13}C- CH_4 is steeper than in GC 52 which hints to a larger contribution of methane from microbial methanogenesis in GC 51. But the change in δ^{13}C-DIC is still

much larger than the change in δ^{13}C- CH_4 which entails a contribution of thermogenic methane.

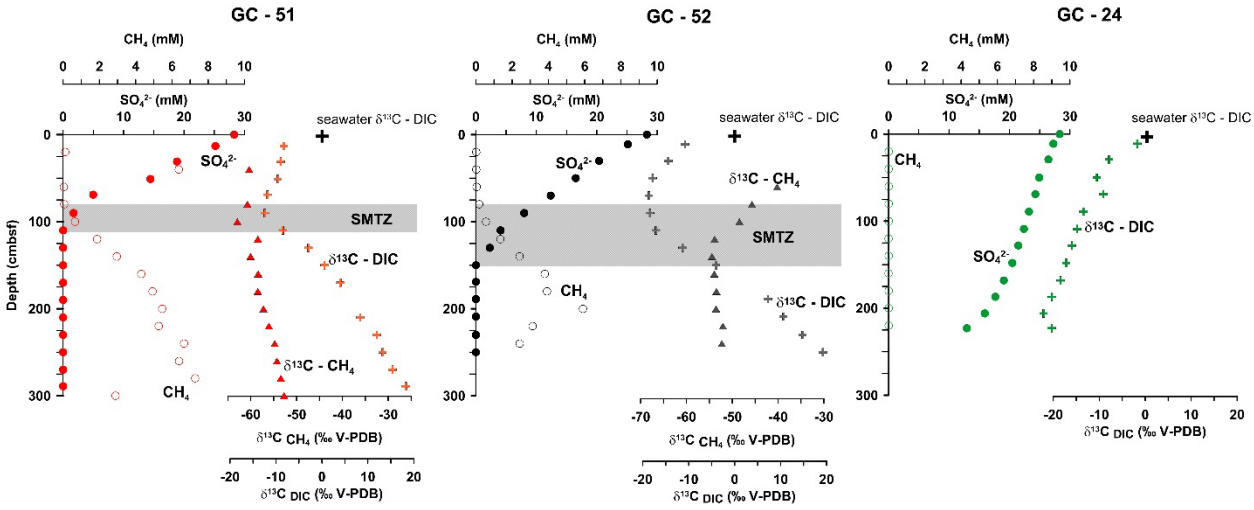

Figure 6: Pore water profiles of sulphate, methane, δ^{13}C-CH_4 and δ^{13}C-DIC in the three gravity cores GC 51, GC 52 and GC 24. The black cross in each graph indicates the δ^{13}C-DIC of seawater (Walter et al., 2007).

5.3.2 δ^{13}C and δ^{2}H of methane

The isotopic composition (δ^{13}C-CH_4) of microbial methane is a function of the active methanogenic population (Katz, 2011) and ranges between -110‰ and -50‰ (Whiticar et al., 1986; Whiticar, 1999). The δ^{13}C-CH_4 of thermogenic methane is generally higher than that of microbial methane and ranges between -50‰ and -20‰, depending on the source rock and maturity of the hydrocarbons (Schoell, 1988; Whiticar, 1999). Whiticar (1999) established a diagram discriminating different methane sources based on their δ^{13}C-CH_4 and δ^{2}H-CH_4 compositions (Fig. 7). The six analysed samples from the Hola area plot on the border between the thermogenic methane field and the mixing field between thermogenic methane and microbial methane produced by carbonate reduction. The high δ^{2}H values (between -191‰ and -225‰) make acetate fermentation an unlikely methane source in our samples (Fig. 7). Thus, according to our results of δ^{13}C and δ^{2}H of methane from sediment cores GC 51 and GC 52, thermogenic methane probably represents the larger proportion of the gas in the Hola area (Fig. 7). Results from GC 52 plot at the margin of the thermogenic field whereas data from GC 51 plot further towards the

microbial methane field. Such differences in δ^{13}C-CH_4 and δ^{2}H-CH_4 compositions between the cores lead to the same conclusion as derived from the depth profiles of δ^{13}C- CH_4 and δ^{13}C-DIC: in both cores the methane is largely of thermogenic origin but in core GC 51 a larger amount of microbial methane is needed than in core GC 52 to account for the measured isotopic values.

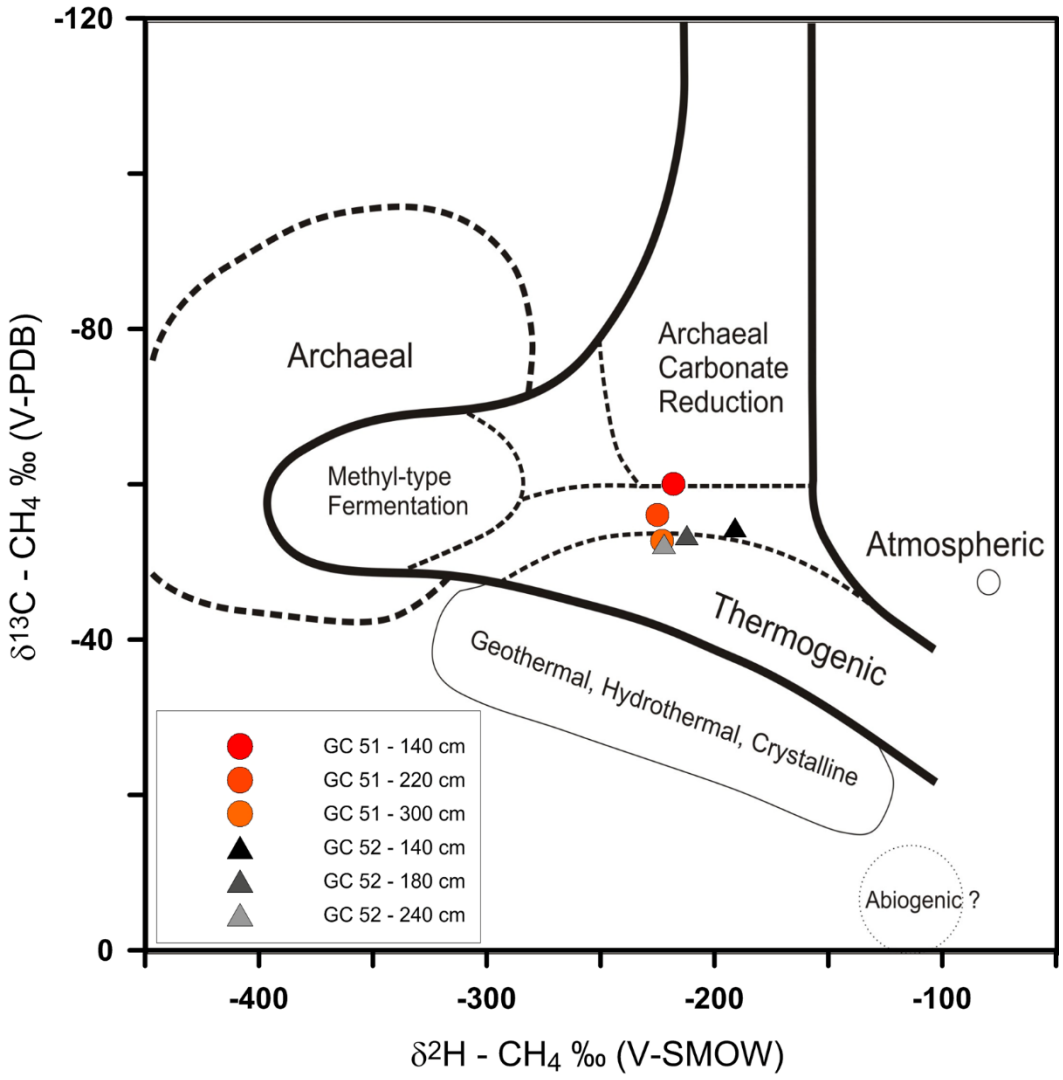

Figure 7: Plot of δ^{13}C-CH_4 against δ^{2}H-CH_4 with fields indicating different methane sources (modified after Whiticar, 1999).Gas compositions from core GC 52 (triangles) plot at the margin of the thermogenic field whereas the results from core GC 51 (dots) indicate a contribution from microbial methanogenesis.

5.3.3 $\delta^{13}C$ of C_1-C_4 hydrocarbons

The predominantly thermogenic source of methane is also supported by the presence and the isotopic composition ($\delta^{13}C$) of the higher molecular weight hydrocarbons. The $\delta^{13}C$ of the individual components of hydrocarbon gases is a function of the mode of formation, precursor composition and alteration processes (Whiticar, 1994). The general pattern of $\delta^{13}C$ of thermogenic C_1-C_4 hydrocarbons is an enrichment in ^{13}C (higher $\delta^{13}C$ values) with increasing molecular mass. This ^{13}C-enrichment is caused by a kinetic fractionation effect during thermogenic gas formation from the high molecular-mass source organic matter (Des Marais et al., 1981; Katz et al., 2002). The $\delta^{13}C$ values of C_1-C_4 hydrocarbons from a thermogenic gas source in the South Caspian basin are plotted in Fig. 8 (Katz et al., 2002) together with our data (average $\delta^{13}C$ for GC 51 and GC 52) that follow the overall trend of the thermogenic gas. However, the $\delta^{13}C$ of methane in the Hola samples is slightly lower than the thermogenic example by around 5‰ and the $\delta^{13}C$ of propane is higher by around 20‰. Also the $\delta^{13}C$ of *n*-butane is slightly enriched. A gas sample from a Pliocene section of the Nile delta (Vandré et al., 2007) shows the nearly same compound-specific isotopic composition as the Hola samples (Fig 8).

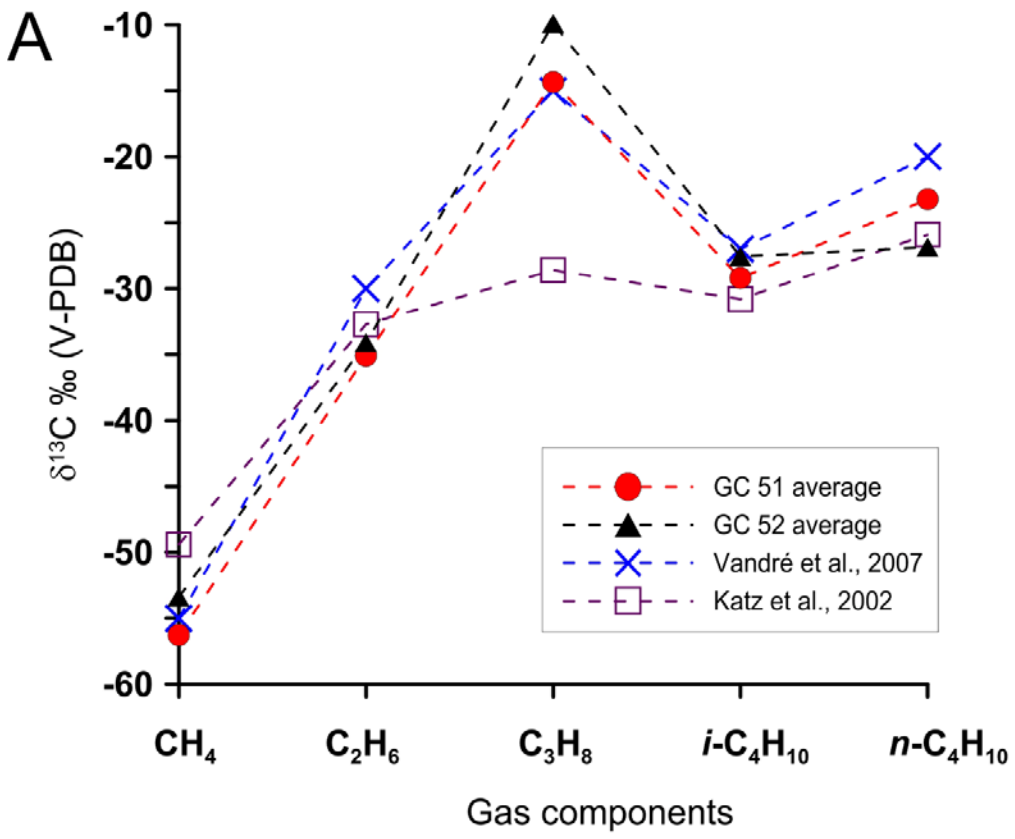

Figure 8: Plot of the average $\delta^{13}C$ of the higher molecular weight hydrocarbons (C1-C4) in our study (GC 51 and GC 52) and values from a thermogenic gas source in the South Caspian basin (Katz et al., 2002) and a gas sample from a Pliocene section of the Nile delta (Vandré et al., 2007).

Vandré et al. (2007) suggest that a small contribution of microbial methane can cause a negative $\delta^{13}C$ shift of methane derived predominantly from a thermogenic source whereas biodegradation of propane can account for the increased $\delta^{13}C$ of propane compared to the thermogenic gas values. This is consistent with findings of James and Burns (1984) showing that in the initial stages of microbial alteration of hydrocarbons propane is preferentially attacked. Microbial degradation of hydrocarbon gases increases the $^{13}C/^{12}C$ ratio in the remaining fraction because breaking ^{12}C-^{12}C bonds requires less energy than breaking ^{13}C-^{12}C bonds (Chung et al., 1988) resulting in isotopic enrichment of propane as

much as 20‰ (James and Burns, 1984). In the Hola samples the $\delta^{13}C$ values of propane are higher by around 18‰ in GC 51 and even 21‰ in GC 52 (assuming a smooth trend from ethane to *i*-butane) which indicates considerable biodegradation of propane in our samples. Furthermore, a preferential degradation of *n*-butane over *i*-butane can be expected (Bopp et al., 1981) which can explain the difference in isotopic composition between these two butane isomers and typically heavier $\delta^{13}C$ values of *n*-butane in studied samples (Fig. 8, Table 2). Similar ^{13}C enrichments of propane and *n*-butane were also reported in sediment porewater above gas hydrates in the Gulf of Mexico (Sassen et al., 2004) and in the fluids of mud volcanoes (Mastalerz et al., 2009). The interpretation of the enriched $\delta^{13}C$ signals of propane and *n*-butane as a sign of biodegradation of these compounds is supported by studies showing that propane and *n*-butane can in fact be anaerobically oxidised (Kniemeyer et al., 2007; Jaekel et al., 2013) by for example sulfate-reducing bacteria.

Combining all the isotope information ($\delta^{13}C$ of C_1-C_4 and $\delta^{2}H$-CH_4), we suggest that the hydrocarbons in the Hola area are predominantly of thermogenic origin probably migrating up from greater depths, and showing signs of biodegradation which caused isotope enrichment in propane and to a small extent in *n*-butane. Furthermore, the isotopic data suggest a contribution of microbial methane, with a larger proportion of microbial methane in core GC 51 than in GC 52.

5.4 Structural controls on hydrocarbon seepage

Nearby the study site a possible source rock for the thermogenic gas was drilled in two wells (6814/04-U-01 and 6814/04-U-02) (Smelror et al., 2001) (Fig. 1 and 3). The wells record crystalline basement overlain by Middle Jurassic to Lower Cretaceous (early Barremian) sediments in the northern Ribban Basin (Hansen et al., 1992; Smelror et al., 2001) (Fig. 9). In well 6418/04-U-01 a few thin but very organic rich mudstone intervals, with a TOC content between 5 and 27%, and coal fragments occur in a

sandstone unit of Middle Jurassic age (Måsnykan Formation) (Fig. 9). The organic matter is immature to early mature with a considerable liquid hydrocarbon potential (Smelror et al., 2001).

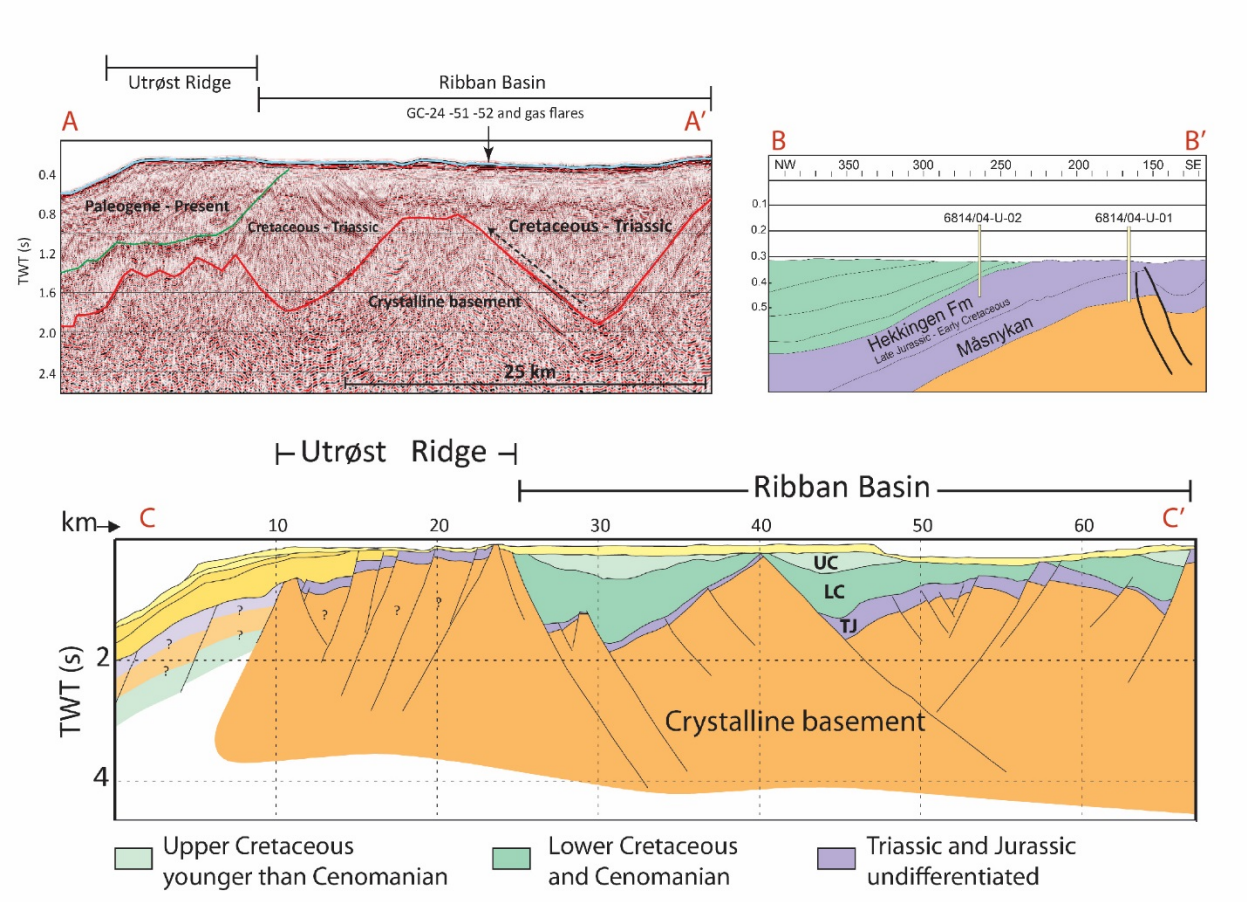

Figure 9: Three cross-shelf seismic lines (location indicated in Fig. 1 and 3) showing the block-faulted nature of the shelf (C-C' profile) (modified after Blystad et al. (1995)), the potential source rock which is part of the Hekkingen Formation (B- B' profile, modified after Smelror et al. (2001)), and the suggested migration pathway along the southeast ward facing flank of the Ribban Basin, marked by a stippled arrow (in the A-A' profile).

Another organic rich, dark, finely laminated silty claystone with a TOC content of 4-9% and a moderate liquid hydrocarbon generation potential was detected in the Alge Member, Upper Jurassic (Hekkingen Formation) (Smelror et al., 2001). In core 6418/04-U-02 the Krill Member (Upper Jurassic to Lower Cretaceous, Hekkingen Formation) contains TOC contents of 2.5% - 4% and has a moderate liquid hydrocarbon generation potential (Smelror et al., 2001). Both the Alge and Krill Member are part of the

Hekkingen Formation, one of the major source rocks along the Norwegian continental margin (Løseth et al., 2011). The distance between the wells and the Hola gas flares is about 30 km and they are located within the same SW-NE trending structure, the Ribban Basin (Fig. 2 and 9). The basin infill spans Triassic/Jurassic to upper Cretaceous sediments and hydrocarbons generated in the Hekkingen Formation may easily migrate along the unconformity above the underlying crystalline basement (Fig. 9). Profile B-B' shows the location of the potential source rocks for the thermogenic gas which are associated with the Hekkingen Formation. This formation probably continues further to the NW down the basin as seen in the C-C' profile and potentially also increases in thickness due to tectonic activity during deposition of this unit (Smelror et al., 2001). A possible migration pathway of the hydrocarbons could be along the south eastward facing flank of the fault block as indicated in Fig. 9, profile A-A'. This is supported by the location of the observed gas flares. From the seismic line, however, it is not possible to infer the complete fluid path all the way to the sediment surface.

6 Conclusions

- Active hydrocarbon seeps were found in the Hola area on the northern Norwegian shelf where ascending methane produces strong heterogeneity in sediment pore water profiles: spatially varying SMTZ depths between 80 cm and > 250 cm indicate focused fluid flow. Furthermore, pore water profiles of Ca show a depletion at the present SMTZ depths suggesting ongoing precipitation of $CaCO_3$ and low ammonium and phosphate concentrations in the pore water point to low rates of organic matter degradation in Hola sediments.
- All isotopic data combined ($\delta^{13}C$ and $\delta^{2}H$ values of methane, $\delta^{13}C$ values of the C_2 to C_4 hydrocarbons and $\delta^{13}C$ of dissolved inorganic carbon) suggest a predominantly thermogenic origin of the Hola gases from a deeper source and furthermore show considerable

biodegradation of propane and to some extent of *n*-butane. The contribution of microbial methane varies in the studied gravity cores.

- Based on 3 seismic profiles and 2 shallow drilling wells a possible late Jurassic to early Cretaceous source rock of the thermogenic gas components is suggested. We conclude that released hydrocarbons have migrated along major unconformities between the basement and overlying Mesozoic sedimentary rocks.

7 Acknowledgments

We thank the captain and the crew of research vessel H.U. Sverdrup II and research vessel Helmer Hansen, including chief scientist Matthias Forwick, for their support during several cruises. We are also grateful to Clea Fabian and Johan Faust for support during sampling at sea. We would further like to thank the NGU laboratory (Trondheim), the Inorganic Geochemistry lab at the Center for Marine Environmental Sciences (Bremen), Prof. Dr. Stefano Bernasconi (ETH Zürich) and Serge Robert (EAWAG) for support during geochemical analyses. The authors acknowledge funding from RWE-Dea (now DEA) and from the Norwegian Research Council through CAGE-Center for Arctic Gas Hydrate, Environment and Climate (grant 223259).

8 References

Aloisi, G., Bouloubassi, I., Heijs, S.K., Pancost, R.D., Pierre, C., Sinninghe Damsté, J.S., Gottschal, J.C., Forney, L.J., Rouchy, J.-M., 2002. CH4-consuming microorganisms and the formation of carbonate crusts at cold seeps. Earth and Planetary Science Letters, 203(1): 195-203.

Alongi, D.M., Wirasantosa, S., Wagey, T., Trott, L.A., 2012. Early diagenetic processes in relation to river discharge and coastal upwelling in the Aru Sea, Indonesia. Marine Chemistry, 140–141(0): 10-23.

Archer, D., Buffett, B., Brovkin, V., 2009. Ocean methane hydrates as a slow tipping point in the global carbon cycle. Proceedings of the National Academy of Sciences, 106(49): 20596-20601.

Bekryaev, R.V., Polyakov, I.V., Alexeev, V.A., 2010. Role of Polar Amplification in Long-Term Surface Air Temperature Variations and Modern Arctic Warming. Journal of Climate, 23(14): 3888-3906.

Bergh, S.G., Eig, K., Kløvjan, O.S., Henningsen, T., Olesen, O., Hansen, J.A., 2007. The Lofoten-Vesterålen continental margin: a multiphase Mesozoic-Palaeogene rifted shelf as shown by offshore-onshore brittle fault-fracture analysis. Norwegian Journal of Geology, 87: 29-58.

Biastoch, A., Treude, T., Rüpke, L.H., Riebesell, U., Roth, C., Burwicz, E.B., Park, W., Latif, M., Böning, C.W., Madec, G., Wallmann, K., 2011. Rising Arctic Ocean temperatures cause gas hydrate destabilization and ocean acidification. Geophysical Research Letters, 38(8): L08602.

Blystad, P., Brekke, H., Færseth, R.B., Larsen, B.T., Skogseid, J., Tørudbakken, B., 1995. Structural Elements of the Norwegian Continental Shelf. Norwegian Petroleum Directorate - Bulletin 8.

Boetius, A., Ravenschlag, K., Schubert, C.J., Rickert, D., Widdel, F., Gieseke, A., Amann, R., Jorgensen, B.B., Witte, U., Pfannkuche, O., 2000. A marine microbial consortium apparently mediating anaerobic oxidation of methane. Nature, 407(6804): 623-626.

Bopp, R.F., Santschi, P.H., Li, Y.-H., Deck, B.L., 1981. Biodegradation and gas-exchange of gaseous alkanes in model estuarine ecosystems. Organic Geochemistry, 3(1–2): 9-14.

Borowski, W.S., Paull, C.K., Ussler, W., 1996. Marine pore-water sulfate profiles indicate in situ methane flux from underlying gas hydrate. Geology, 24(7): 655-658.

Bünz, S., Polyanov, S., Vadakkepuliyambatta, S., Consolaro, C., Mienert, J., 2012. Active gas venting through hydrate-bearing sediments on the Vestnesa Ridge, offshore W-Svalbard. Marine Geology, 332–334(0): 189-197.

Bøe, R., Bellec, V.K., Dolan, M.F.J., Buhl-Mortensen, P., Buhl-Mortensen, L., Slagstad, D., Rise, L., 2009. Giant sandwaves in the Hola glacial trough off Vesterålen, North Norway. Marine Geology, 267(1–2): 36-54.

Canfield, D.E., 1991. Sulfate reduction in deep-sea sediments. American Journal of Science, 291(2): 177-188.

Chand, S., Rise, L., Bellec, V., Dolan, M., Bøe, R., Thorsnes, T., Buhl-Mortensen, P., 2008. Active Venting System Offshore Northern Norway. Eos, Transactions American Geophysical Union, 89(29): 261-262.

Chand, S., Thorsnes, T., Rise, L., Brunstad, H., Stoddart, D., Bøe, R., Lågstad, P., Svolsbru, T., 2012. Multiple episodes of fluid flow in the SW Barents Sea (Loppa High) evidenced by gas flares, pockmarks and gas hydrate accumulation. Earth and Planetary Science Letters, 331–332(0): 305-314.

Chen, Y., Ussler III, W., Haflidason, H., Lepland, A., Rise, L., Hovland, M., Hjelstuen, B.O., 2010. Sources of methane inferred from pore-water δ13C of dissolved inorganic carbon in Pockmark G11, offshore Mid-Norway. Chemical Geology, 275(3–4): 127-138.

Chung, H.M., Gormly, J.R., Squires, R.M., 1988. Origin of gaseous hydrocarbons in subsurface environments: Theoretical considerations of carbon isotope distribution. Chemical Geology, 71(1–3): 97-104.

Claypool, G., Kaplan, I.R., 1974. The Origin and Distribution of Methane in Marine Sediments. In: Kaplan, I. (Ed.), Natural Gases in Marine Sediments. Marine Science. Springer US, pp. 99-139.

Cline, J.D., 1969. Spectrophotometric determination of hydrogen sulfide in natural waters. Limnology and Oceanography, 14: 454 - 458.

Collins, P.F., Diehl, H., Smith, G.F., 1959. 2,4,6-Tripyridyl-s-triazine as Reagent for Iron. Determination of Iron in Limestone, Silicates, and Refractories. Analytical Chemistry, 31(11): 1862-1867.

Damm, E., Mackensen, A., Budéus, G., Faber, E., Hanfland, C., 2005. Pathways of methane in seawater: Plume spreading in an Arctic shelf environment (SW-Spitsbergen). Continental Shelf Research, 25(12–13): 1453-1472.

Des Marais, D.J., Donchin, J.H., Nehring, N.L., Truesdell, A.H., 1981. Molecular carbon isotopic evidence for the origin of geothermal hydrocarbons. Nature, 292(5826): 826-828.

Feng, D., Birgel, D., Peckmann, J., Roberts, H.H., Joye, S.B., Sassen, R., Liu, X.-L., Hinrichs, K.-U., Chen, D., 2014. Time integrated variation of sources of fluids and seepage dynamics archived in authigenic carbonates from Gulf of Mexico Gas Hydrate Seafloor Observatory. Chemical Geology, 385: 129-139.

Fischer, D., Sahling, H., Nöthen, K., Bohrmann, G., Zabel, M., Kasten, S., 2012. Interaction between hydrocarbon seepage, chemosynthetic communities, and bottom water redox at cold seeps of the Makran accretionary prism: insights from habitat-specific pore water sampling and modeling. Biogeosciences, 9(6): 2013-2031.

Froelich, P.N., Klinkhammer, G.P., Bender, M.L., Luedtke, N.A., Heath, G.R., Cullen, D., Dauphin, P., Hammond, D., Hartman, B., Maynard, V., 1979. Early oxidation of organic matter in pelagic sediments of the eastern equatorial Atlantic: suboxic diagenesis. Geochimica et Cosmochimica Acta, 43(7): 1075-1090.

Færseth, R.B., 2012. Structural development of the continental shelf offshore Lofoten–Vesterålen, northern Norway. Norwegian Journal of Geology, 92: 19-40.

Gieskes, J., Mahn, C., Day, S., Martin, J.B., Greinert, J., Rathburn, T., McAdoo, B., 2005. A study of the chemistry of pore fluids and authigenic carbonates in methane seep environments: Kodiak Trench, Hydrate Ridge, Monterey Bay, and Eel River Basin. Chemical Geology, 220(3–4): 329-345.

Goericke, R., Fry, B., 1994. Variations of marine plankton δ13C with latitude, temperature, and dissolved CO2 in the world ocean. Global Biogeochemical Cycles, 8(1): 85-90.

Haeckel, M., König, I., Riech, V., Weber, M.E., Suess, E., 2001. Pore water profiles and numerical modelling of biogeochemical processes in Peru Basin deep-sea sediments. Deep Sea Research Part II: Topical Studies in Oceanography, 48(17–18): 3713-3736.

Hall, P.O.J., Aller, R.C., 1992. Rapid, small-volume, flow injection analysis for C02, and NH4+ in marine and freshwaters. Limnology and Oceanography, 35: 1113-1119.

Hansen, J.W., Bakke, S., Fanavoll, S., 1992. Shallow drilling Nordland VI and VII 1991. IKU Report, 23.

Henningsen, T., Tveten, E., 1998. Berggrunnskart ANDØYA, M 1:250 000. Norges Geologiske Undersøkelse, Trondheim.

Hensen, C., Zabel, M., Pfeifer, K., Schwenk, T., Kasten, S., Riedinger, N., Schulz, H.D., Boetius, A., 2003. Control of sulfate pore-water profiles by sedimentary events and the significance of anaerobic oxidation of methane for the burial of sulfur in marine sediments. Geochimica et Cosmochimica Acta, 67(14): 2631-2647.

Hesselbo, S.P., Grocke, D.R., Jenkyns, H.C., Bjerrum, C.J., Farrimond, P., Morgans Bell, H.S., Green, O.R., 2000. Massive dissociation of gas hydrate during a Jurassic oceanic anoxic event. Nature, 406(6794): 392-395.

Heuer, V.B., Pohlman, J.W., Torres, M.E., Elvert, M., Hinrichs, K.-U., 2009. The stable carbon isotope biogeochemistry of acetate and other dissolved carbon species in deep subseafloor sediments at the northern Cascadia Margin. Geochimica et Cosmochimica Acta, 73(11): 3323-3336.

Hinrichs, K.-U., Hayes, J.M., Sylva, S.P., Brewer, P.G., DeLong, E.F., 1999. Methane-consuming archaebacteria in marine sediments. Nature, 398(6730): 802-805.

Hovland, M., Judd, A.G., 1988. Seabed Pockmarks and Seepages. Impact on Geology, Biology and Marine Environment. Graham & Trotman London, Dordrecht, Boston, 293 pp.

Hustoft, S., Bünz, S., Mienert, J., Chand, S., 2009. Gas hydrate reservoir and active methane-venting province in sediments on < 20 Ma young oceanic crust in the Fram Strait, offshore NW-Svalbard. Earth and Planetary Science Letters, 284(1–2): 12-24.

Iversen, N., Jørgensen, B.B., 1985. Anaerobic methane oxidation rates at the sulfate-methane transition in marine sediments from Kattegat and Skagerrak (Denmark) 1. Limnology and Oceanography, 30(5): 944-955.

Jaekel, U., Musat, N., Adam, B., Kuypers, M., Grundmann, O., Musat, F., 2013. Anaerobic degradation of propane and butane by sulfate-reducing bacteria enriched from marine hydrocarbon cold seeps. ISME J, 7(5): 885-895.

James, A.T., Burns, B.J., 1984. Microbial alteration of subsurface natural gas accumulations. AAPG Bulletin, 68(8): 957-960.

Judd, A., 2004. Natural seabed gas seeps as sources of atmospheric methane. Environmental Geology, 46(8): 988-996.

Katz, B.J., Narimanov, A., Huseinzadeh, R., 2002. Significance of microbial processes in gases of the South Caspian basin. Marine and Petroleum Geology, 19(6): 783-796.

Katz, B.J., 2011. Microbial Processes and Natural Gas Accumulations. The Open Geology Journal, 5: 75-83.

Katz, M.E., Pak, D.K., Dickens, G.R., Miller, K.G., 1999. The Source and Fate of Massive Carbon Input During the Latest Paleocene Thermal Maximum. Science, 286(5444): 1531-1533.

Kniemeyer, O., Musat, F., Sievert, S.M., Knittel, K., Wilkes, H., Blumenberg, M., Michaelis, W., Classen, A., Bolm, C., Joye, S.B., Widdel, F., 2007. Anaerobic oxidation of short-chain hydrocarbons by marine sulphate-reducing bacteria. Nature, 449(7164): 898-901.

Lammers, S., Suess, E., Hovland, M., 1995. A large methane plume east of Bear Island (Barents Sea): implications for the marine methane cycle. Geologische Rundschau, 84(1): 59-66.

Libes, S., 2009. Introduction to Marine Biogeochemistry Elsevier Academic Press, 928 pp.

Loeseth, H., Tveten, E., 1996. Post-Caledonian structural evolution of the Lofoten and Vesteralen offshore and onshore areas. Norwegian Journal of Geology, 76: 215-230.

Luff, R., Wallmann, K., 2003. Fluid flow, methane fluxes, carbonate precipitation and biogeochemical turnover in gas hydrate-bearing sediments at Hydrate Ridge, Cascadia Margin: numerical modeling and mass balances. Geochimica et Cosmochimica Acta, 67(18): 3403-3421.

Løseth, H., 1999. Paleogeographical evolution of the Lofoten and Vesterålen onshore and offshore area, Geonytt, Abstract volume, pp. 71-72.

Løseth, H., Wensaas, L., Gading, M., Duffaut, K., Springer, M., 2011. Can hydrocarbon source rocks be identified on seismic data? Geology, 39(12): 1167-1170.

Mastalerz, V., de Lange, G.J., Dählmann, A., 2009. Differential aerobic and anaerobic oxidation of hydrocarbon gases discharged at mud volcanoes in the Nile deep-sea fan. Geochimica et Cosmochimica Acta, 73(13): 3849-3863.

Mazurenko, L.L., Soloviev, V.A., 2003. Worldwide distribution of deep-water fluid venting and potential occurrences of gas hydrate accumulations. Geo-Marine Letters, 23(3-4): 162-176.

McGinnis, D.F., Greinert, J., Artemov, Y., Beaubien, S.E., Wüest, A., 2006. Fate of rising methane bubbles in stratified waters: How much methane reaches the atmosphere? Journal of Geophysical Research: Oceans, 111(C9): C09007.

Moore, T.S., Murray, R.W., Kurtz, A.C., Schrag, D.P., 2004. Anaerobic methane oxidation and the formation of dolomite. Earth and Planetary Science Letters, 229(1–2): 141-154.

Murphy, J., Riley, J.P., 1962. A modified single solution method for the determination of phosphate in natural waters. Analytica Chimica Acta, 27(0): 31-36.

Niewöhner, C., Hensen, C., Kasten, S., Zabel, M., Schulz, H.D., 1998. Deep Sulfate Reduction Completely Mediated by Anaerobic Methane Oxidation in Sediments of the Upwelling Area off Namibia. Geochimica et Cosmochimica Acta, 62(3): 455-464.

Orcutt, B., Boetius, A., Elvert, M., Samarkin, V., Joye, S.B., 2005. Molecular biogeochemistry of sulfate reduction, methanogenesis and the anaerobic oxidation of methane at Gulf of Mexico cold seeps. Geochimica et Cosmochimica Acta, 69(17): 4267-4281.

Orphan, V.J., House, C.H., Hinrichs, K.-U., McKeegan, K.D., DeLong, E.F., 2001. Methane-Consuming Archaea Revealed by Directly Coupled Isotopic and Phylogenetic Analysis. Science, 293(5529): 484-487.

Ottesen, D., Dowdeswell, J.A., Rise, L., Rokoengen, K., Henriksen, S., 2002. Large-scale morphological evidence for past ice-stream flow on the mid-Norwegian continental margin. Geological Society, London, Special Publications, 203(1): 245-258.

Ottesen, D., Dowdeswell, J.A., Rise, L., 2005a. Submarine landforms and the reconstruction of fast-flowing ice streams within a large Quaternary ice sheet: The 2500-km-long Norwegian-Svalbard margin (57°–80°N). Geological Society of America Bulletin, 117(7-8): 1033-1050.

Ottesen, D., Rise, L., Knies, J., Olsen, L., Henriksen, S., 2005b. The Vestfjorden-Trænadjupet palaeo-ice stream drainage system, mid-Norwegian continental shelf. Marine Geology, 218(1–4): 175-189.

Portnov, A., Smith, A.J., Mienert, J., Cherkashov, G., Rekant, P., Semenov, P., Serov, P., Vanshtein, B., 2013. Offshore permafrost decay and massive seabed methane escape in water depths >20 m at the South Kara Sea shelf. Geophysical Research Letters, 40(15): 3962-3967.

Punshon, S., Azetsu-Scott, K., Lee, C.M., 2014. On the distribution of dissolved methane in Davis Strait, North Atlantic Ocean. Marine Chemistry, 161(0): 20-25.

Reeburgh, W.S., 1976. Methane consumption in Cariaco Trench waters and sediments. Earth and Planetary Science Letters, 28(3): 337-344.

Rice, D.D., Claypool, G.E., 1981. Generation, Accumulation, and Resource Potential of Biogenic Gas. AAPG Bulletin, 65: 5-25.

Rise, L., Chand, S., Haflidason, H., L'Heureux, J., Hjelstuen, B., Bellec, V., Longva, O., Brendryen, J., Vanneste, M., Bøe, R., 2012. Investigations of Slides at the Upper Continental Slope Off Vesterålen, North Norway. In: Yamada, Y. et al. (Eds.), Submarine Mass Movements and Their Consequences. Advances in Natural and Technological Hazards Research. Springer Netherlands, pp. 167-176.

Sahling, H., Römer, M., Pape, T., Bergès, B., dos Santos Fereirra, C., Boelmann, J., Geprägs, P., Tomczyk, M., Nowald, N., Dimmler, W., Schroedter, L., Glockzin, M., Bohrmann, G., 2014. Gas emissions at the continental margin west of Svalbard: mapping, sampling, and quantification. Biogeosciences, 11(21): 6029-6046.

Sassen, R., Roberts, H.H., Carney, R., Milkov, A.V., DeFreitas, D.A., Lanoil, B., Zhang, C., 2004. Free hydrocarbon gas, gas hydrate, and authigenic minerals in chemosynthetic communities of the northern Gulf of Mexico continental slope: relation to microbial processes. Chemical Geology, 205(3–4): 195-217.

Sauter, E.J., Muyakshin, S.I., Charlou, J.-L., Schlüter, M., Boetius, A., Jerosch, K., Damm, E., Foucher, J.-P., Klages, M., 2006. Methane discharge from a deep-sea submarine mud volcano into the upper

water column by gas hydrate-coated methane bubbles. Earth and Planetary Science Letters, 243(3–4): 354-365.

Schoell, M., 1988. Multiple origins of methane in the Earth. Chemical Geology, 71(1–3): 1-10.

Schulz, H.D., 2006. Quantification of Early Diagenesis: Dissolved Constituents in Pore Water and Signals in the Solid Phase. In: Schulz, H.D., Zabel, M. (Eds.), Marine Geochemistry. Springer Berlin Heidelberg, pp. 73-124.

Shakhova, N., Semiletov, I., Salyuk, A., Yusupov, V., Kosmach, D., Gustafsson, Ö., 2010. Extensive Methane Venting to the Atmosphere from Sediments of the East Siberian Arctic Shelf. Science, 327(5970): 1246-1250.

Skarke, A., Ruppel, C., Kodis, M., Brothers, D., Lobecker, E., 2014. Widespread methane leakage from the sea floor on the northern US Atlantic margin. Nature Geoscience, 7(9): 657-661.

Smelror, M., Mørk, A., Mørk, M.B.E., Weiss, H.M., Løseth, H., 2001. Middle jurassic-lower cretaceous transgressive-regressive sequences and facies distribution off northern nordland and troms, Norway. In: Ole, J.M., Tom, D. (Eds.), Norwegian Petroleum Society Special Publications: Sedimentary Environments Offshore Norway — Palaeozoic to Recent. Elsevier, pp. 211-232.

Solheim, A., Larsson, F.R., 1987. Seismic indications of shallow gas in the Northern Barents Sea.

Suess, E., Torres, M.E., Bohrmann, G., Collier, R.W., Greinert, J., Linke, P., Rehder, G., Trehu, A., Wallmann, K., Winckler, G., Zuleger, E., 1999. Gas hydrate destabilization: enhanced dewatering, benthic material turnover and large methane plumes at the Cascadia convergent margin. Earth and Planetary Science Letters, 170(1): 1-15.

Ussler III, W., Paull, C.K., 2008. Rates of anaerobic oxidation of methane and authigenic carbonate mineralization in methane-rich deep-sea sediments inferred from models and geochemical profiles. Earth and Planetary Science Letters, 266(3–4): 271-287.

Valentine, D.L., Blanton, D.C., Reeburgh, W.S., Kastner, M., 2001. Water column methane oxidation adjacent to an area of active hydrate dissociation, Eel river Basin. Geochimica et Cosmochimica Acta, 65(16): 2633-2640.

Vandré, C., Cramer, B., Gerling, P., Winsemann, J., 2007. Natural gas formation in the western Nile delta (Eastern Mediterranean): Thermogenic versus microbial. Organic Geochemistry, 38(4): 523-539.

Vorren, T.O., Vorren, K.-D., Aasheim, O., Dahlgren, K.I.T., Forwick, M., Hassel, K., 2013. Palaeoenvironment in northern Norway between 22.2 and 14.5 cal. ka BP. Boreas, 42(4): 876-895.

Vorren, T.O., Rydningen, T.A., Baeten, N.J., Laberg, J.S., 2015. Chronology and extent of the Lofoten–Vesterålen sector of the Scandinavian Ice Sheet from 26 to 16 cal. ka BP. Boreas: Advance online publication.

Walter, L.M., Ku, T.C.W., Muehlenbachs, K., Patterson, W.P., Bonnell, L., 2007. Controls on the δ13C of dissolved inorganic carbon in marine pore waters: An integrated case study of isotope exchange during syndepositional recrystallization of biogenic carbonate sediments (South Florida Platform, USA). Deep-Sea Research Part II, 54(11-13): 1163-1200.

Wehrmann, L.M., Risgaard-Petersen, N., Schrum, H.N., Walsh, E.A., Huh, Y., Ikehara, M., Pierre, C., D'Hondt, S., Ferdelman, T.G., Ravelo, A.C., Takahashi, K., Zarikian, C.A., 2011. Coupled organic and inorganic carbon cycling in the deep subseafloor sediment of the northeastern Bering Sea Slope (IODP Exp. 323). Chemical Geology, 284(3–4): 251-261.

Westbrook, G.K., Thatcher, K.E., Rohling, E.J., Piotrowski, A.M., Pälike, H., Osborne, A.H., Nisbet, E.G., Minshull, T.A., Lanoisellé, M., James, R.H., Hühnerbach, V., Green, D., Fisher, R.E., Crocker, A.J., Chabert, A., Bolton, C., Beszczynska-Möller, A., Berndt, C., Aquilina, A., 2009. Escape of methane gas from the seabed along the West Spitsbergen continental margin. Geophysical Research Letters, 36(15): L15608.

Whiticar, M., 1994. Correlation of natural gases with their sources. In: Magoon, L.B., Dow, W.G. (Eds.), The Petroleum System – From Source to Trap. American Association of Petroleum Geologists Memoir, pp. 261 - 283.

Whiticar, M.J., Faber, E., Schoell, M., 1986. Biogenic methane formation in marine and freshwater environments: CO2 reduction vs. acetate fermentation—Isotope evidence. Geochimica et Cosmochimica Acta, 50(5): 693-709.

Whiticar, M.J., 1999. Carbon and hydrogen isotope systematics of bacterial formation and oxidation of methane. Chemical Geology, 161(1–3): 291-314.

Yamamoto, S., Alcauskas, J.B., Crozier, T.E., 1976. Solubility of methane in distilled water and seawater. Journal of Chemical & Engineering Data, 21(1): 78-80.

9 Data

Table 3: Temperature, salinity and oxygen concentration results from CTD 209

water depth (m)	Temp (°C)	Salinity (‰)	O_2 (ml/l)
1.0	6.22	34.59	5.77
2.0	6.17	34.59	5.77
3.0	6.17	34.59	5.77
4.0	6.17	34.59	5.77
5.0	6.17	34.59	5.78
5.9	6.17	34.59	5.78
6.9	6.17	34.59	5.77
7.9	6.17	34.59	5.77
8.9	6.16	34.59	5.76
9.9	6.16	34.59	5.77
10.9	6.17	34.59	5.77
11.9	6.17	34.59	5.78
12.9	6.17	34.59	5.77
13.9	6.17	34.59	5.77
14.8	6.17	34.59	5.77
15.8	6.17	34.59	5.77
16.8	6.17	34.59	5.76
17.8	6.17	34.59	5.74
18.8	6.18	34.59	5.73
19.8	6.18	34.59	5.73
20.8	6.19	34.59	5.73
21.8	6.20	34.60	5.73
22.8	6.21	34.60	5.73
23.7	6.22	34.60	5.74
24.7	6.22	34.60	5.74
25.7	6.22	34.60	5.72
26.7	6.22	34.60	5.70
27.7	6.22	34.60	5.70
28.7	6.22	34.60	5.70
29.7	6.22	34.60	5.69
30.7	6.23	34.61	5.69
31.7	6.24	34.61	5.69
32.7	6.24	34.61	5.68
33.7	6.24	34.61	5.67
34.6	6.24	34.61	5.67
35.6	6.24	34.61	5.69
36.6	6.25	34.61	5.70
37.6	6.25	34.61	5.70
38.6	6.25	34.61	5.69
39.6	6.24	34.61	5.70
40.6	6.24	34.61	5.70
41.6	6.24	34.61	5.70
42.6	6.24	34.61	5.70
43.6	6.24	34.61	5.70
44.5	6.25	34.61	5.70
45.5	6.25	34.61	5.67
46.5	6.25	34.61	5.67
47.5	6.25	34.61	5.67
48.5	6.25	34.61	5.65
49.5	6.26	34.62	5.63
50.5	6.26	34.62	5.64
51.5	6.26	34.62	5.65
52.5	6.26	34.61	5.66
53.4	6.26	34.61	5.65
54.4	6.26	34.61	5.64
55.4	6.26	34.61	5.64
56.4	6.26	34.61	5.64
57.4	6.27	34.62	5.64
58.4	6.27	34.62	5.64
59.4	6.27	34.62	5.65
60.4	6.27	34.62	5.64
61.4	6.27	34.62	5.64
62.4	6.27	34.62	5.65
63.3	6.27	34.62	5.64
64.3	6.27	34.62	5.63
65.3	6.28	34.62	5.63
66.3	6.27	34.62	5.63
67.3	6.27	34.62	5.64
68.3	6.27	34.62	5.65
69.3	6.28	34.62	5.66
70.3	6.28	34.62	5.67
71.3	6.28	34.62	5.68
72.3	6.28	34.62	5.67
73.2	6.27	34.62	5.65
74.2	6.26	34.61	5.65
75.2	6.26	34.61	5.64
76.2	6.27	34.62	5.63
77.2	6.27	34.61	5.62
78.2	6.27	34.62	5.61
79.2	6.27	34.62	5.61
80.2	6.27	34.62	5.60
81.2	6.28	34.62	5.58
82.1	6.28	34.62	5.58
83.1	6.28	34.62	5.59
84.1	6.29	34.62	5.61
85.1	6.30	34.63	5.62
86.1	6.31	34.63	5.61
87.1	6.31	34.63	5.59
88.1	6.31	34.63	5.58
89.1	6.32	34.63	5.58
90.1	6.33	34.63	5.57
91.0	6.32	34.63	5.56
92.0	6.32	34.63	5.56
93.0	6.33	34.63	5.57
94.0	6.33	34.63	5.57
95.0	6.33	34.63	5.57
96.0	6.33	34.63	5.56
97.0	6.33	34.63	5.56
98.0	6.33	34.64	5.55
99.0	6.34	34.64	5.56
100.0	6.34	34.64	5.57
100.9	6.34	34.64	5.55

Table 1 continued: Temperature, salinity and oxygen concentration results from CTD 209

water depth (m)	Temp (°C)	Salinity (‰)	O_2 (ml/l)
101.9	6.33	34.64	5.54
102.9	6.34	34.64	5.54
103.9	6.34	34.64	5.53
104.9	6.35	34.64	5.54
105.9	6.35	34.64	5.55
106.9	6.35	34.64	5.57
107.9	6.35	34.64	5.56
108.9	6.35	34.64	5.55
109.9	6.35	34.64	5.54
110.8	6.35	34.64	5.55
111.8	6.35	34.64	5.56
112.8	6.35	34.64	5.56
113.8	6.35	34.64	5.57
114.8	6.35	34.64	5.58
115.8	6.35	34.64	5.59
116.8	6.36	34.65	5.58
117.8	6.35	34.65	5.57
118.8	6.36	34.65	5.59
119.7	6.36	34.65	5.58
120.7	6.36	34.65	5.58
121.7	6.36	34.65	5.57
122.7	6.36	34.65	5.55
123.7	6.36	34.65	5.55
124.7	6.36	34.65	5.54
125.7	6.36	34.65	5.54
126.7	6.36	34.65	5.56
127.7	6.36	34.65	5.57
128.7	6.36	34.65	5.58
129.6	6.36	34.65	5.57
130.6	6.36	34.65	5.56
131.6	6.36	34.65	5.55
132.6	6.36	34.65	5.54
133.6	6.36	34.65	5.55
134.6	6.36	34.65	5.56
135.6	6.36	34.65	5.57
136.6	6.36	34.65	5.56
137.6	6.36	34.65	5.55
138.5	6.36	34.65	5.55
139.5	6.36	34.65	5.57
140.5	6.36	34.65	5.58
141.5	6.36	34.65	5.58
142.5	6.36	34.65	5.56
143.5	6.37	34.65	5.56
144.5	6.36	34.65	5.55
145.5	6.37	34.65	5.54
146.5	6.37	34.65	5.55
147.4	6.37	34.65	5.54
148.4	6.37	34.65	5.54
149.4	6.37	34.65	5.54
150.4	6.37	34.65	5.56
151.4	6.37	34.65	5.57
152.4	6.38	34.66	5.56
153.4	6.37	34.65	5.56
154.4	6.38	34.66	5.56
155.3	6.38	34.66	5.55
156.4	6.38	34.66	5.54
157.3	6.38	34.66	5.52
158.3	6.38	34.65	5.52
159.3	6.38	34.65	5.52
160.3	6.38	34.66	5.52
161.3	6.39	34.66	5.53
162.3	6.40	34.66	5.53
163.3	6.40	34.67	5.52
164.3	6.41	34.67	5.52
165.3	6.41	34.67	5.52
166.2	6.43	34.68	5.52
167.2	6.43	34.68	5.51
168.2	6.44	34.68	5.50
169.2	6.45	34.68	5.50
170.2	6.46	34.69	5.50
171.2	6.46	34.69	5.50
172.2	6.47	34.69	5.49
173.2	6.47	34.70	5.48
174.2	6.48	34.70	5.50
175.1	6.49	34.71	5.51
176.1	6.50	34.71	5.52
177.1	6.51	34.72	5.51
178.1	6.51	34.72	5.50
179.1	6.51	34.72	5.49
180.1	6.51	34.72	5.50
181.1	6.51	34.72	5.50
182.1	6.52	34.72	5.50
183.1	6.53	34.73	5.49
184.0	6.56	34.74	5.46
185.0	6.56	34.74	5.47
186.0	6.57	34.75	5.48
187.0	6.57	34.75	5.48
188.0	6.60	34.76	5.47
189.0	6.63	34.77	5.45
190.0	6.63	34.78	5.45
191.0	6.63	34.77	5.45
192.0	6.65	34.78	5.45
193.0	6.66	34.79	5.45
193.9	6.67	34.80	5.46
194.9	6.68	34.80	5.45
195.9	6.68	34.80	5.45
196.9	6.68	34.80	5.44
197.9	6.69	34.80	5.44
198.9	6.69	34.80	5.44
199.9	6.70	34.81	5.42
200.9	6.72	34.82	5.41
201.9	6.75	34.83	5.40
202.8	6.78	34.84	5.39
203.8	6.80	34.85	5.39
204.8	6.81	34.86	5.40
205.8	6.81	34.86	5.41
206.8	6.81	34.86	5.41
207.8	6.81	34.86	5.39
208.8	6.81	34.86	5.39
209.8	6.81	34.86	5.39
210.7	6.81	34.86	5.38
211.7	6.82	34.86	5.38
212.7	6.82	34.86	5.38
213.7	6.82	34.86	5.39
214.7	6.82	34.86	5.39
215.7	6.82	34.86	5.38

Table 4: Dissolved methane concentrations in the water column

CTD 209	Water depth (m)	CH_4 (nM)
	50	20.3
	200	21.7
	210	32.8
	215	42.7

Table 5: Results of pore water and gas analyses of cores GC 24, GC 51 and GC 52

GC-24	Depth (cm)	PO_4^{3-} (µM)	SO_4^{2-} (mM)	Cl^- (mM)	NH_4^+ (µM)	HS^- (mM)	Fe^{2+} (µM)	Ca^{2+} (mM)	$\delta^{13}C$- DIC (‰ V-PDB)	Depth (cm)	CH_4 (µM)	$\delta^{13}C$- CH_4 (‰ V-PDB)	δ^2H- CH_4 (‰ V-SMOW)
	0	0.7	28.3	537.5	6.1	< 0.001	< 0.05	9.7	-	-	-	-	-
	11	8.2	27.3	525.8	2.5	< 0.001	21.8	9.8	-2	20	4.2	-	-
	29	10.3	26.4	528.3	24.3	< 0.001	42.0	9.2	-8	40	6.6	-	-
	50	10.5	24.9	519.8	38.8	< 0.001	42.2	9.1	-11	60	5.0	-	-
	69	10.7	24.3	528.6	38.8	< 0.001	44.5	-	-9	80	7.4	-	-
	89	12.1	23.2	527.7	53.3	< 0.001	46.3	-	-13	100	7.8	-	-
	109	13.4	22.4	535.8	67.8	< 0.001	57.0	7.6	-15	120	3.3	-	-
	128	15.0	21.5	532.9	75.0	< 0.001	54.8	7.7	-16	140	3.7	-	-
	148	16.2	20.5	531.5	82.3	< 0.001	53.6	7.4	-17	160	0.6	-	-
	168	15.5	19.1	522.7	96.8	< 0.001	49.7	7.1	-18	180	11.5	-	-
	187	12.6	17.7	523.1	111.3	< 0.001	28.7	6.5	-20	200	9.9	-	-
	206	13.5	15.9	534.3	125.8	< 0.001	15.4	6.0	-22	220	7.8	-	-
	223	10.9	13.0	529.2	154.8	< 0.001	1.2	4.9	-20	-	-	-	-

GC-51	Depth (cm)	PO_4^{3-} (µM)	SO_4^{2-} (mM)	Cl^- (mM)	NH_4^+ (µM)	HS^- (mM)	Fe^{2+} (µM)	Ca^{2+} (mM)	$\delta^{13}C$- DIC (‰ V-PDB)	Depth (cm)	CH_4 (mM)	$\delta^{13}C$- CH_4 (‰ V-PDB)	δ^2H- CH_4 (‰ V-SMOW)
	0	0.7	28.3	537.5	6.1		< 0.05	9.7	-	-	-	-	-
	13	15.1	25.2	535.4	24.3	0.4	< 0.05	9.6	-8	20	0.1	-	-
	31	23.7	18.8	538.7	53.3	2.2	< 0.05	8.0	-9	40	8.0	-60	-
	51	24.2	14.5	528.4	67.8	3.0	< 0.05	6.9	-10	60	0.05	-	-
	69	28.5	5.0	533.8	96.8	6.3	< 0.05	4.7	-12	80	0.1	-61	-
	90	33.3	1.7	540.2	111.3	7.1	< 0.05	4.3	-12	100	0.8	-63	-
	110	38.5	< 0.07	529.3	115.6	6.5	< 0.05	4.4	-8	120	2.3	-58	-
	130	46.2	< 0.07	536.8	140.3	5.2	< 0.05	4.5	-3	140	3.7	-60	-218
	150	51.9	< 0.07	534.2	176.5	3.8	< 0.05	4.7	1	160	5.4	-58	-
	170	56.7	< 0.07	525.7	186.7	2.6	0.1	4.8	4	180	6.2	-58	-
	190	56.8	< 0.07	490.1	186.7	0.8	< 0.05	-	-	200	6.8	-57	-
	210	66.2	< 0.07	529.3	198.3	0.1	0.1	5.1	8	220	6.6	-56	-225
	230	66.7	< 0.07	531.6	227.3	< 0.001	0.1	5.3	12	240	8.3	-55	-
	250	64.3	< 0.07	533.6	227.3	< 0.001	2.0	5.6	13	260	8.0	-54	-
	270	53.8	< 0.07	536.3	227.3	< 0.001	41.2	5.6	15	280	9.1	-53	-
	289	53.8	< 0.07	530.6			26.4	5.8	18	300	3.6	-53	-223

GC-52	Depth (cm)	PO_4^{3-} (µM)	SO_4^{2-} (mM)	Cl^- (mM)	NH_4^+ (µM)	HS^- (mM)	Fe^{2+} (µM)	Ca^{2+} (mM)	$\delta^{13}C$- DIC (‰ V-PDB)	Depth (cm)	CH_4 (mM)	$\delta^{13}C$- CH_4 (‰ V-PDB)	δ^2H- CH_4 (‰ V-SMOW)
	0	0.7	28.3	537.5	6.1		< 0.05	9.7	-	-	-	-	-
	11	15.1	25.1	537.0	24.3	0.5	< 0.05	9.1	-11	20	0.03	-	-
	30	16.6	20.4	538.3		1.2	< 0.05	7.9	-14	40	0.03	-	-
	50	17.0	16.5	536.5	38.8	2.3	< 0.05	6.8	-18	60	0.05	-40	-
	70	16.6	12.4	537.8	38.8	3.3	< 0.05	5.9	-19	80	0.2	-46	-
	90	15.6	8.0	535.4	53.3	4.8	< 0.05	4.7	-18	100	0.7	-48	-
	110	19.0	4.1	531.3	60.5	5.8	< 0.05	4.0	-17	120	1.7	-54	-
	130	19.0	2.3	529.7	67.8	5.1	< 0.05	3.5	-11	140	3.0	-54	-191
	150	21.3	< 0.07	529.2	82.3	4.3	0.1	3.5	-4	160	4.8	-54	-
	169	22.5	< 0.07	533.9	96.8	0.1	0.2	3.9	-	180	4.9	-53	-212
	189	25.2	< 0.07	535.0	82.3	0.9	0.1	4.2	7	200	7.4	-54	-
	209	25.6	< 0.07	534.2	125.8	0.1	0.2	4.6	11	220	3.9	-52	-
	230	23.0	< 0.07	542.2	140.3	< 0.001	54.3	5.1	15	240	3.0	-52	-222
	250	16.1	< 0.07	526.1	154.8	< 0.001	67.5	5.2	19				

Table 6: Carbon and hydrogen stable isotope results of methane, ethane, propane and butane of cores GC 51 and GC 52

	δ^2H (‰ V-SMOW)	δ^{13}C (‰ V-PDB)				
Sample	CH_4	CH_4 (C_1)	C_2H_6 (C_2)	C_3H_8 (C_3)	*i*-C_4H_{10} (*i*-C_4)	*n*-C_4H_{10} (*n*-C_4)
GC 51-140 cm	-218	-60.0	-34.4	-14.9	-29.4	-22.4
GC 51-220 cm	-225	-56.1	-36.5	-16	-28.8	-22.5
GC 51-300 cm	-223	-52.7	-34.4	-12.1	-29.4	-24.8
GC 52-140 cm	-191	-54.4	-33.7	-9.5	-29.7	-25.2
GC 52-180 cm	-212	-53.5	-34.6	-13.2	-26.0	-26.3
GC 52-240 cm	-222	-52.3	-34.0	-7.0	-27.0	-29.1